

# Universal Time Variations in the Magnetosphere and the Effect of CME Arrival Time: Analysis of the February 2022 Event that Led to the Loss of Starlink Satellites

M. Lockwood<sup>1</sup>, M.J. Owens<sup>1</sup>, and L.A. Barnard<sup>1</sup>

<sup>1</sup>Department of Meteorology, University of Reading, Reading, Berkshire, RG6 6BB, UK

## Key Points:

- Analysis of the CME effects causing the loss of 38 Starlink satellites shows that the terrestrial response to a CME depends on its impact  $UT$
- $UT$  effects are caused by diurnal motions of the poles and the eccentric nature of the geomagnetic field
- Joule heating dominated in the southern polar cap during the first CME and initially during the second but later was dominant in the north

---

Corresponding author: Mike Lockwood, [m.lockwood@reading.ac.uk](mailto:m.lockwood@reading.ac.uk)

This article has been accepted for publication and undergone full peer review but has not been through the copyediting, typesetting, pagination and proofreading process, which may lead to differences between this version and the [Version of Record](#). Please cite this article as [doi: 10.1029/2022JA031177](https://doi.org/10.1029/2022JA031177).

This article is protected by copyright. All rights reserved.

Accepted Article

## Abstract

We study Universal Time ( $UT$ ) variations in the magnetospheric response to Coronal Mass Ejection (CME) impacts, using the example of the two CMEs that led to the destruction of 38 out of 49 Starlink satellites in early February 2022. We employ the Expanding-Contracting Polar Cap model to analyse the variation in the size of the ionospheric polar caps and an eccentric dipole model of the geomagnetic field and thereby quantify the  $UT$  variations caused by the inductive effect of the diurnal motions of the geomagnetic poles in a “geocentric-solar” frame of reference (i.e., a frame with an X axis that points from the centre of the Earth to the centre of the Sun). The results show that use of a quasi-steady convection model predicts a similar global power deposition into the thermosphere as that inferred here, but does not give the same division of that power between the northern and southern hemispheres. We demonstrate that, through the combined effects of the Russell-McPherron dipole-tilt mechanism on solar-wind magnetosphere coupling and of the diurnal polar cap motions in a geocentric-solar frame, the power deposited varies significantly with the arrival  $UT$  of the CMEs at Earth. We also show that in the events of early February 2022, both CMEs arrived at almost the optimum  $UT$  to cause maximum thermospheric heating.

## Plain Language Summary

We use a recent well-publicised space-weather event as an example of a previously-overlooked aspect of the behaviour of near-Earth space. The event took place in early February 2022, when 38 out of 49 Starlink satellites burned up in Earth’s atmosphere because two Coronal Mass Ejections (CMEs) emitted from the Sun hit the Earth and had a larger heating effect on the upper atmosphere than expected. The new element that we introduce is the effect of the eccentricity of Earth’s magnetic field which is reflected in the offset of the magnetic pole from the geographic pole being considerably greater in the southern hemisphere than in the northern hemisphere. This introduces a daily variation into the response of Earth’s magnetosphere to a given solar wind disturbance and we show that the effect would have been less severe during the February 2022 event had the CMEs arrived either earlier or later than they did.

## 1 Introduction

### 1.1 The events of 3-4 February, 2022

The impact of two Coronal Mass Ejections (CMEs) on Earth’s magnetosphere on 3 and 4 February 2022 caused the loss of 38 of 49 recently-launched SpaceX Starlink satellites due to enhanced upper atmosphere density during the resulting geomagnetic storm. (Hapgood et al., 2022; Fang et al., 2022; Kataoka et al., 2022; Tsurutani et al., 2022; Y. Zhang et al., 2022; Dang et al., 2022). The full financial cost of this space weather event is not known but has been estimated to be upward of \$20m for the lost satellites and \$30m for the wasted launch capacity. A surprising element of this event is that the causal geomagnetic disturbance was moderately large but not extreme. The global geomagnetic activity  $Kp$  index reached a value of 5+ after the impact of each CME, a value exceeded 3.5% of the time since production of the  $Kp$  index began in 1932 (Bartels et al., 1939; Bartels, 1949). This level meant that the event was classified as a minor storm according to the scale used by NOAA’s Space Weather Prediction Centre (SWPC). The 3-hourly global  $am$  geomagnetic index (Mayaud, 1972) indicates a slightly rarer event, reaching 84nT after both CMEs - a level that is exceeded 2% of the time since the  $am$  index data series began in January 1959.

On 3 February 2022, at 18:13 UTC, the Starlink satellites had been launched by a SpaceX Falcon 9 rocket from NASA’s Kennedy Space Center in Florida into an orbit with perigee of 210 km. This was the 36th in a series of such launches since May 2019.

63 However the geomagnetic storm, which at the time of launch had just begun, subsequently  
64 raised the density of the atmosphere, increasing the drag on the satellites and induced  
65 re-entry before the planned deployment of electric thrusters could raise all but 11 of them  
66 to an operational orbit at altitude near 500 km. Consequently, 38 of the 49 satellites burnt  
67 up in the atmosphere on 7 February. SpaceX has responded to the loss by changing its  
68 launch procedures: the subsequent Starlink launch on 21 February used a higher initial  
69 orbit at 300 km altitude, but carried only 46 instead of 49 satellites. It should be noted  
70 that SpaceX's adoption of a low initial orbit is good and responsible strategy: if a satel-  
71 lite fails initial checks it can be readily de-orbited from such a low altitude and so does  
72 not add to the accumulation of space junk. However, it is a strategy that places the satel-  
73 lites at risk from space weather-driven changes in atmospheric drag, which is what hap-  
74 pened to the ill-fated satellites launched on 3 February. The event clearly demonstrates  
75 one of several reasons why it is important to link responsible procedures to minimise space  
76 junk with space weather forecasting (Hapgood et al., 2022).

77 Several recent papers have studied the science behind this event. Fang et al. (2022)  
78 have looked at the CMEs causing the event, their propagation from Sun to Earth and  
79 their forecasting using the standard tools of a 3-dimensional MHD model of the helio-  
80 sphere, based on solar magnetograph data, with a CME "cone model", which is inserted  
81 based on coronagraph images of the event eruptions. It appears from this analysis that  
82 forecasts used by the SpaceX launch team underestimated the scale of thermospheric heat-  
83 ing, and consequent density rises at the initial satellite orbit, that the event caused. For  
84 example, the standard empirical NRLMSISE-00 model (Picone et al., 2002) predicts a  
85 rise of only about 5% in neutral density at 210 km. Limb observations during the event  
86 indicate that the actual rise at 210 km was between 11% and 18% on the dusk side of  
87 the low-latitude Earth and 40% to 59% on the the dawn side (Y. Zhang et al., 2022).  
88 Dang et al. (2022) predict somewhat smaller rises in thermospheric densities than some  
89 other studies but show that the integrated effect on the satellites was still enough to cause  
90 re-entry from 210 km altitude. On the other hand, Kataoka et al. (2022) suggest the heat-  
91 ing effect was greater and more widespread and the study by Tsurutani et al. (2022) of  
92 orbit changes from other satellites, such as Swarm, suggests the thermospheric density  
93 changes were large and the Starlink satellite orbits did not decay as fast as this would  
94 predict because they had been partially lifted from their initial orbit.

95 The thermospheric modelling by Dang et al. (2022) used the National Center for  
96 Atmospheric Research (NCAR) Thermosphere Ionosphere Electrodynamics General Cir-  
97 culation Model (TIEGCM), a three-dimensional, self-consistent, physical model of the  
98 coupled ionosphere-thermosphere system (Richmond et al., 1992). For very quiet times  
99 particle precipitation seems to dominate magnetospheric energy deposition in the ionosphere-  
100 thermosphere system; however, for small storms, the Joule heating by the ionospheric  
101 E-region Pedersen currents associated with F-region convection (X. Zhang et al., 2005;  
102 Kalafatoglu et al., 2018) is slightly larger than that due to particle precipitation, and for  
103 large storms Joule heating is dominant (Wilson et al., 2006; Robinson & Zanetti, 2021;  
104 Hajra et al., 2022). To define the Joule heating input to the coupled thermosphere-ionosphere  
105 model, Dang et al. (2022) employed the empirical convection and Joule heating model  
106 of Weimer (2005) which uses the prevailing solar wind and IMF conditions and assumes  
107 a steady-state response of the magnetosphere with only directly-driven energy deposi-  
108 tion.

## 109 1.2 Polar cap Expansion and Contraction and Universal Time effects

110 In this paper, we look at the magnetospheric behaviour during the February 2022  
111 events. In general, some of the energy extracted from the solar wind by the magneto-  
112 sphere is directly deposited in the polar upper atmosphere by currents and precipitat-  
113 ing particles, whereas a second component is stored in the geomagnetic tail and deposited  
114 after a delay (Baker et al., 1997; Shukhtina et al., 2005; Blockx et al., 2009; Liu et al.,

115 2018). The energy is largely stored as magnetic energy of open flux in the tail and so  
 116 the cycle of energy storage and release is reflected in the open flux,  $F_{PC}$ . However,  $F_{PC}$   
 117 is not a perfect indicator of energy stored because the lobe magnetic energy density is  
 118 proportional to the square of the magnetic field in the lobe, which can be increased in  
 119 the near-Earth tail for a given  $F_{PC}$  by the squeezing effect of enhanced solar wind dy-  
 120 namic pressure (Caan et al., 1973; Lockwood, McWilliams, et al., 2020; Lockwood, Owens,  
 121 Barnard, Watt, et al., 2020). Nevertheless, because the ionospheric field  $B_i$  is effectively  
 122 constant, changes in the area of the region of ionospheric open flux (here termed the pol-  
 123 ar cap),  $A_{PC} = F_{PC}/B_i$ , indicate the energy storage in, and release from, the tail. The  
 124 next section discusses the Expanding-Contracting Polar Cap (ECPC) model and how  
 125 the expansion and contraction of the polar cap relates to ionospheric F-region convec-  
 126 tion voltages (Cowley & Lockwood, 1992; Lockwood & Cowley, 2022), and the associ-  
 127 ated E-region Pedersen currents and hence energy dissipation in the ionosphere and ther-  
 128 mosphere by Joule heating. By using the ECPC model, in which the open flux rises and  
 129 falls, we separate the energy deposition by the directly-driven system from that by the  
 130 storage-release system, whereas if steady state is assumed (i.e., with constant  $F_{PC}$ ) there  
 131 is only directly-driven power dissipation and one is ignoring the existence of the storage-  
 132 release system. There is not room here to review the literature on the relative impor-  
 133 tance of directly-driven and storage-release energy deposition in the ionosphere and ther-  
 134 mosphere; however, we can say that both observations and global MHD modelling show  
 135 that the storage-release system is certainly not negligible, is often dominant and cannot  
 136 be ignored (Shukhtina et al., 2005; Blockx et al., 2009; Liu et al., 2018).

137 Another factor that we investigate in the present paper is the effect on cycles of  
 138 energy storage and dissipation of motions of the magnetic poles in any “geocentric-solar”  
 139 frame of reference, caused by Earth’s rotation (Lockwood et al., 2021). By geocentric-  
 140 solar, we mean any frame with an X axis that points from the center of the Earth to the  
 141 center of the Sun, such as GSE (Geocentric Solar Ecliptic), GSEQ (Geocentric Solar Equa-  
 142 torial) of GSM (Geocentric Solar Magnetospheric). These introduce Universal Time (UT)  
 143 variations which are close to being in antiphase in the two hemispheres and which are  
 144 larger in the southern hemisphere because the offset of the magnetic and rotational poles  
 145 is greater. Lockwood and Milan (2023) have recently reviewed causes and observations  
 146 of  $UT$  effects in the magnetosphere, as seen in averages from long-term datasets. These  
 147 include global geomagnetic indices, auroral electrojet indices, partial ring current indices,  
 148 transpolar voltage data and field-aligned current data from the AMPERE project, ex-  
 149 ploiting magnetometers on board the Iridium swarm of 70 satellites.

150 An often-discussed potential effect of pole motions on energy deposition is that of  
 151 ionospheric conductivity variations. Enhanced conductivity, generated by solar EUV il-  
 152 lumination, peaks when the polar cap is tipped towards the Sun whereas the pole-motion  
 153 voltage effect peaks six hours earlier when the pole is tipping towards the Sun at its fastest  
 154 rate. For the February period studied here, calculations of the mean conductivity in the  
 155 northern polar cap and auroral ovals show almost no variation with  $UT$  as almost all  
 156 of those regions is on the nightside (solar zenith angles,  $\chi > 100^\circ$ ) all of the time. On  
 157 the other hand, there is a considerable quasi-sinusoidal  $UT$  variation in conductivity for  
 158 the southern polar cap and auroral oval as most of those regions is subjected to diur-  
 159 nal variations in zenith angles  $\chi$  below  $90^\circ$  that induce major conductivity changes (Ridley  
 160 et al., 2004).

161 However, there are a number of points that need to be considered about effects of  
 162 variations in this solar-EUV-induced conductivity in the polar cap and auroral oval. Much  
 163 of the energy dissipation during geomagnetic storms takes place in the auroral ovals, caused  
 164 by the Pedersen currents that connect the Region 1 and Region 2 field-aligned currents  
 165 and where conductivity is dominated by auroral precipitation rather than being gener-  
 166 ated by solar EUV (Carter et al., 2020). This greatly reduces the significance of the so-  
 167 lar EUV generated conductivity to energy deposition during geomagnetic storms. In ad-

168 dition,  $UT$  effects are introduced into heating rates by the neutral wind velocity (Cai  
169 et al., 2014; Billett et al., 2018), but we note that regular diurnal effects due to neutral  
170 winds are less clear in disturbed times when the convection pattern is changing faster  
171 than the neutral wind can respond.

172 There is also a need to be consistent when evaluating the roles of ionospheric con-  
173 ductivity and flux transport, a need that is imposed by Maxwell's equation  $\nabla \cdot \mathbf{B} = 0$ .  
174 The point being that this fundamental equation of electromagnetism (the non-existence  
175 of magnetic monopoles) demands that the open flux in the two hemispheres must be iden-  
176 tical because it is generated and lost by magnetic reconnections which affect both hemi-  
177 spheres (as opposed to reconnection between field in one lobe and a northward interplan-  
178 etary field which causes a circulation in that lobe and polar cap but does not change  $F_{PC}$ ).  
179 In addition, when averaged over sufficient time, the antisunward magnetic flux transport  
180 rate of open flux in both ionospheric polar caps (i.e. the transpolar voltages) must be  
181 the same as that of the parts of the open field lines that are in interplanetary space. The  
182 latter cannot be influenced by ionospheric conductivity because the antisunward flow there  
183 is supersonic and super-Alfvénic. The same is true for most of the tail magnetosheath  
184 (Li et al., 2020). Several numerical simulations show that increased polar cap conduc-  
185 tivity reduces transpolar voltages (e.g., Borovsky et al., 2009). This is expected as field-  
186 perpendicular conductivities (both Hall and Pedersen) arise from collisions between ions  
187 and electrons and neutral atoms and ion-neutral collisions also give frictional drag on  
188 the motion of F-region plasma and frozen-in magnetic field (Ridley et al., 2004). As dis-  
189 cussed by Tanaka (2007) and (for an isolated flux tube) by Southwood (1987), this is the  
190 “line-tying” concept introduced by Atkinson (1967, 1978) to explain the origin of field-  
191 aligned currents and how they transfer momentum and energy down into the ionosphere.  
192 Because the interplanetary segments of open field lines, outside the bow shock in the “Stern  
193 gap”, and indeed in the tail magnetosheath, are flowing supersonically and super-Alfvénically  
194 away from the ionospheric polar cap that they are connected to, they can have no in-  
195 formation about the state of the ionosphere and so are not influenced in any way by the  
196 slowing of their field line footpoints. Hence the reduction in transpolar voltage associ-  
197 ated with enhanced polar cap conductivity must give induction effects in the field of the  
198 relevant tail lobe between the ionosphere and the tail magnetopause and hence a rise in  
199 the energy stored in that field. This means that enhanced conductivity is really influ-  
200 encing the balance between energy stored in the tail (and later released) and energy di-  
201 rectly deposited in the ionosphere. Some (we will define it to be a fraction  $f_L$ ) of the en-  
202 ergy stored by the inductive field changes that decouple the ionospheric transpolar vol-  
203 tage and the Stern gap voltage, may be in the tail and antisunward of the reconnection  
204 X-line in the cross-tail current sheet that closes open flux: this part of the stored energy  
205 will be lost to the near-Earth magnetosphere and the ionosphere/thermosphere and re-  
206 turned to the solar wind. On the other hand, the remainder (a fraction  $1 - f_L$ ) of the  
207 energy stored by the inductive field changes will be sunward of the tail reconnection X-  
208 line and that stored energy is deposited by Joule and particle heating via the storage-  
209 release system and in the ECPC, associated with the nightside reconnection voltage.

210 Because the resistance to motion of open field lines is in the ionosphere, almost all  
211 of any induced field changes and extra energy storage will be in the near-Earth magne-  
212 tosphere and  $f_L$  will be very small. This means that if transpolar voltage in a given po-  
213 lar cap is reduced by enhanced polar cap conductivity (resulting in the associated directly-  
214 driven energy deposition in the ionosphere and thermosphere being reduced), after a de-  
215 lay (typically a substorm growth phase duration) the lost energy is deposited by the flows  
216 and associated Joule heating accompanying the enhanced nightside reconnection as part  
217 of the storage-release system. Hence “saturation” effects associated with enhanced iono-  
218 spheric conductivity which limit the transpolar voltage and Joule dissipation (X. Zhang  
219 et al., 2005) do not cause a reduction in total flux transport seen in the ionosphere, but  
220 they do spread it out over a longer time interval via the storage/release system and this  
221 will have a corresponding effect on the variation in Joule heating. Hence if we were to

include modulation of the directly-driven transpolar voltage by ionospheric EUV-generated conductivity effects, we would also need to modulate the storage-release system in an appropriate way which requires knowledge of the tail lobe field changes.

In theory, this can be achieved using a full global MHD model of the magnetosphere, but here we do not include EUV-induced conductivity effects on transpolar voltage in the summer (southern) hemisphere because to modulate the directly-driven system without including a matching modulation of the storage-release system would be an inconsistent analysis. In addition, we argue that for the dominant energy deposition in the auroral oval, conductivity induced by particle precipitation dominates over that due to solar EUV photoionization.

## 2 Theory and Methods

### 2.1 Polar cap Expansion and Contraction

Two key parameters in the analysis presented in this paper are the dawn-dusk diameters of the ionospheric polar caps,  $d_{PC}$ , and the voltage placed across them by the solar wind flow, the transpolar voltage,  $\Phi_{PC}$  (also referred to as the cross-cap potential drop and synonymous with the polar cap flux transport rate). We investigate the variation of both using the Expanding-Contracting Polar Cap (ECPC) model (Cowley & Lockwood, 1992; Lockwood & Cowley, 2022). Continuity of open flux is the core equation of the ECPC model and is equivalent to Faraday’s law (in integral form) applied to the open-closed field line boundary:

$$dF_{PC}/dt = \Phi_D - \Phi_N \quad (1)$$

where  $F_{PC}$  is the magnetospheric open flux,  $\Phi_D$  is the reconnection voltage in the dayside magnetopause (the rate of production of open flux) and  $\Phi_N$  is the reconnection voltage in the nightside, cross-tail current sheet (the rate of loss of open flux).

We here adopt the major simplifying assumption that the ionospheric open-flux polar caps remain circular. This is certainly not valid all of the time, particularly for strongly and prolonged northward IMF when  $F_{PC}$  is well below its average value of about  $0.4GWb$ . In such cases, a “horse-collar” auroral form is often seen, indicating a teardrop-shaped open flux region (Hones et al., 1989; Elphinstone et al., 1993; Imber et al., 2006; Milan et al., 2020; Bower et al., 2022; Wang et al., 2022). Nevertheless, the assumption of a circular polar cap has been successfully used many times with the ECPC model (e.g., Lockwood et al., 1990; Milan et al., 2017), including an analysis of a full year of data (Milan et al., 2021) and has two major advantages for the present study. Firstly the transpolar voltage is given by (Lockwood, 1991; Connor et al., 2014; Milan et al., 2017, 2021)

$$\Phi_{PC} = (\Phi_D + \Phi_N)/2 + \Phi_V \quad (2)$$

where  $\Phi_V$  is the sum of the voltages induced by all viscous-like (non-reconnection) mechanisms. Secondly this assumption allows us to relate the flux  $F_{PC}$  and diameter  $d_{PC}$  of the polar cap. We use Equation 4 of Milan et al. (2021) which they employ to derive the open flux  $F_{PC}$  by integration of the vertical ionospheric field  $B_i$  inside the polar cap from the latitude of the region 1 field-aligned currents using a model geomagnetic field with an offset of the circular polar cap centre from the magnetic pole towards the nightside of  $4^\circ$ . These authors find the values  $F_{PC}$  are insensitive to this offset in the range  $1^\circ$  -  $10^\circ$ . We remove the latitudinal offset of  $\Delta\Lambda = 4^\circ$  between the open-closed boundary and the region 1 currents that Milan et al. employed and express the latitudinal radius in terms of the open flux polar cap diameter, an arc length,  $d_{PC}$  at an altitude of  $400km$ :

$$F_{PC} = (3.259 \times 10^{-5})d_{PC}^2 + 23.53d_{PC} - (2.7 \times 10^7) \quad (3)$$

where  $F_{PC}$  is in  $Wb$  and  $d_{PC}$  is in  $m$ .

Note that subtle changes in the shape of the open polar cap are a key part of understanding the pattern of ionospheric convection, as predicted by the ECPC model (Lockwood et al., 1990; Cowley & Lockwood, 1992; Lockwood & Morley, 2004; Lockwood, Lanchester, et al., 2006; Lockwood & Cowley, 2022; Tulegenov et al., 2023), particularly in determining the pattern of flow following a burst in either the magnetopause or the tail reconnection voltages. However, the distortions to the boundary, and the flow patterns associated with them, propagate around the boundary (Morley & Lockwood, 2005). These transient features, and others associated with filamentary field-aligned currents caused by dynamic pressure pulse impacts on the magnetosphere (Lhr et al., 1996), are therefore not part of the present paper because of the simplifying assumption of a circular polar cap.

When using the ECPC it is important to understand the importance of the timescale  $\tau$  over which the data are averaged. If a large  $\tau$  is used, this is averaging over many cycles of expansion and contraction of the polar cap and  $dF_{PC}/dt$  tends to zero. From Equation 1 this steady-state condition means that  $\langle \Phi_N \rangle_\tau = \langle \Phi_D \rangle_\tau$ . Only for small  $\tau$  do we see the full expansion and contraction of the polar cap. Increasing  $\tau$  causes the analysis to tend towards steady state. An important timescale in this is  $\tau \sim 1hr$ , which is close to the average duration of the substorm cycle. In such cycles, although much of the open flux generated in the growth phase (by enhanced magnetopause reconnection voltage  $\Phi_D$ ) can be lost in the subsequent expansion and recovery phases by enhanced reconnection voltage in the cross-tail current sheet,  $\Phi_N$ , one substorm cycle does not generally return the polar cap flux to the value it had at the start of the growth phase. It can take a string of weakening substorm expansions to achieve that (Lockwood & McWilliams, 2021b). Conversely, some substorms deposit more energy than was stored in the growth phase leaving the stored tail energy at a lower level than it was at the start of that growth phase (Baker et al., 1997). Furthermore there are steady convection intervals (Lockwood et al., 2009) and intervals of driven convection (Milan et al., 2021) which can last considerably longer than an hour. Later in this paper we demonstrate that the first CME in the February 2022 event is an example of how large, persistent and increasing  $\Phi_D$  prevents  $\Phi_N$  establishing a steady-state, despite several substorm expansions, even on averaging timescales of 1-2 days. In general, the voltage  $\Phi_D$  is constantly changing because of the variability in the solar wind parameters (Lockwood, Bentley, et al., 2019; Lockwood, 2022; Lockwood & Cowley, 2022). As a result, although steady state is a good approximation for  $\tau$  of several days, we can still detect the effects of non-steady behaviour at  $\tau = 1hr$ , although they will be reduced in magnitude by the averaging.

## 2.2 Determination of the magnetopause reconnection voltage, $\Phi_D$

Lockwood and McWilliams (2021b) used a dataset of 25 years of hourly-averaged data ( $\tau = 1hr$ ) to show that the optimum solar wind coupling function depends on which magnetospheric response index it is aimed at predicting. In particular, they showed that the coupling function that best predicts transpolar voltage  $\Phi_{PC}$  is considerably different from those that best predict geomagnetic activity indices. Best practice in deriving these coupling functions was discussed by these authors and by Lockwood (2022). In particular, the results of regression and correlation analysis tends to be weighted towards the means of the distributions and the fit often underestimates the full range and extreme values of the observations (Lockwood, Rouillard, et al., 2006; Sivadas & Sibeck, 2022). The method used by Lockwood and McWilliams (2021b) and Lockwood (2022) avoids this by fitting to averages in bins that cover the full range, meaning that the weighting is equal across the whole range of the data and not dominated by the larger number of

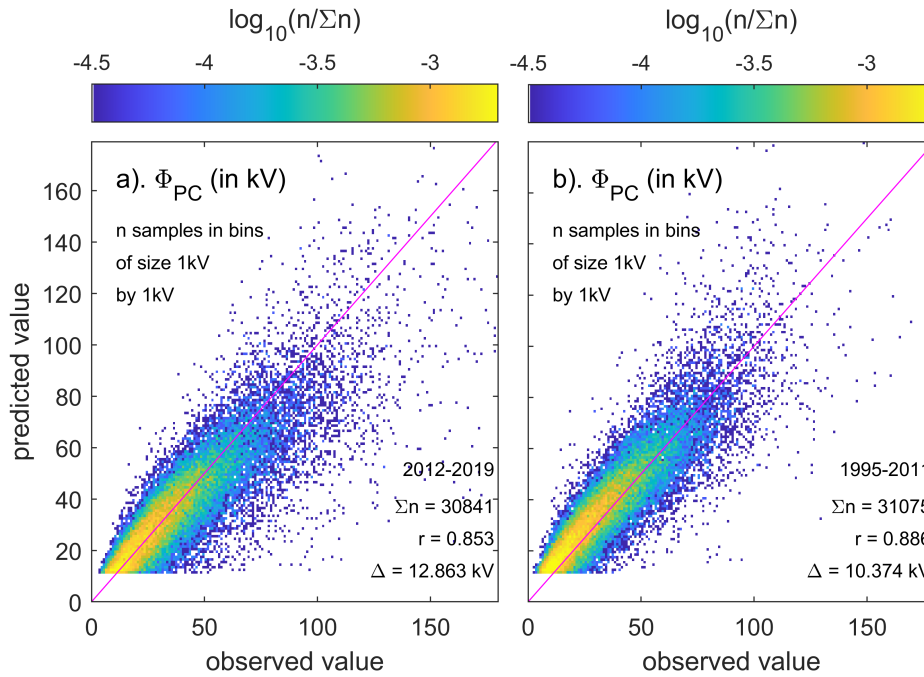


**Figure 1.** Scatter plots of observed and predicted hourly means of transpolar voltage,  $\Phi_{PC}$ . The observations are from the survey of 25 years' data from the northern hemisphere coherent-scatter SuperDARN radar network by Lockwood and McWilliams (2021b). The predicted values are made using the interplanetary data in the Omni2 dataset (King & Papitashvili, 2005), using the procedure described by Lockwood and McWilliams (2021a) to generate a coupling function for transpolar voltage (see Equation 4 of text). (a) is for the fit data subset (2012-2019, inclusive) and (b) for the independent test data subset (1995-2011, inclusive). In both panels the fraction of valid samples,  $n/\Sigma n$ , is color-coded on a logarithmic scale as a function of observed and predicted transpolar voltage, in bins of size  $1kV$  by  $1kV$  with  $n \geq 3$  samples. The total number of samples,  $\Sigma n$ , the correlation coefficient,  $r$ , and the r.m.s. deviation of fitted from observed values,  $\Delta$ , are given. The mauve line are perfect agreement of observed and predicted  $\Phi_{PC}$ .

315 data points close to the mean. There are also pitfalls over time resolution (Laundal et  
 316 al., 2020; Lockwood, 2022). Figure 1 demonstrates the best-fit coupling function to the  
 317 transpolar voltage observed by the SuperDARN coherent radar network and shows that  
 318 another major pitfall, overfitting, has been avoided because the fit is essentially the same  
 319 for the independent test half of the dataset than for the fit data subset that was used  
 320 in the derivation of the coupling function. Overfitting is a problem that is particularly  
 321 facilitated by the presence of datagaps in the interplanetary data which were a serious  
 322 but neglected problem for coupling function studies using data from before the advent  
 323 of the near-continuous data from the ACE and Wind interplanetary monitors in 1995.  
 324 The best way to handle data gaps has been discussed by Finch and Lockwood (2007)  
 325 and Lockwood, Bentley, et al. (2019). In both cases shown in Figure 1, an optimum lag  
 326 of 20min of  $\Phi_{PC}$  behind the interplanetary coupling function is employed (see Figure  
 327 6 of Lockwood & McWilliams, 2021b).

328 The mauve line in Figure 1 is an average fit to many years of data, which means  
 329 that steady-state applies to the fitted value so that, from Equation 2,  $\langle\Phi_D\rangle = \langle\Phi_N\rangle =$   
 330  $\langle\Phi_{PC} - \Phi_V\rangle$ . The best-fit is given by:

$$\langle\Phi_{PC}\rangle = \langle\Phi_D\rangle + \langle\Phi_V\rangle = s_T[B_{\perp}^a \rho_{sw}^b V_{sw}^c \sin^d(\theta/2)] + i_T \quad (4)$$

331 where:  $B_{\perp} = (B_Y^2 + B_Z^2)^{1/2}$  is the IMF transverse to the  $X$  direction of the GSM  
 332 frame (in nT);  $\rho_{sw}$  is the solar wind mass density (in  $\text{kg cm}^{-3}$ );  $V_{sw}$  is the  $X$ -component  
 333 of the solar wind velocity (in  $\text{km s}^{-1}$ ),  $\theta = \tan^{-1}(|B_Y|/|B_Z|)$  is the IMF clock angle in  
 334 the GSM frame and  $B_Y$  and  $B_Z$  are the  $Y$  and  $Z$  IMF components in that frame. The  
 335 best-fit constants are  $a = 0.6554$ ,  $b = 0.0522$ ,  $c = 0.6676$ ,  $d = 2.5$ ,  $i_T = 13.5\text{kV}$  and  $s_T = 8.4075$   
 336 for the above parameter units and  $\Phi_{PC}$  in kV. The above parameters give an root-mean-  
 337 square error (RMSE) of  $\Delta = 12.863\text{kV}$  for the fit data set (Figure 1a) and of  $\Delta = 10.347\text{kV}$   
 338 for the test data set (Figure 1b). Given that the viscous-like voltage is not predicted to  
 339 have the dependence on the IMF clock angle, we here take  $\Phi_V$  to be equal to  $i_T = 13.5\text{kV}$ ,  
 340 a value reasonably consistent with studies by both ground-based radars and satellite ob-  
 341 servations at the flank magnetopause (Lockwood & McWilliams, 2021b; Hapgood & Lock-  
 342 wood, 1993). Hence

$$\Phi_D = s_T[B_{\perp}^a \rho_{sw}^b V_{sw}^c \sin^d(\theta/2)] \quad (5)$$

343 Equation 5 is derived from hourly means. We studied the relationship between the  
 344 1-minute values of  $\Phi_D$  computed using this equation and a variety of one-minute geo-  
 345 magnetic indices ( $SML$ ,  $SMU$ ,  $AL$ ,  $AU$ ,  $SMR$  and  $SYM-H$ ) at the optimum lag and com-  
 346 pared it with that for 1-hour running means of the same data. The correlation is nat-  
 347 urally lower for the 1-minute data (e.g., for  $-SML$  0.66 as opposed to 0.80) in each case  
 348 as the scatter is greater, but the best-fit polynomial is almost identical for the two time  
 349 resolutions in all cases. Hence we here use Equation 5 to generate 1-minute values of  $\Phi_D$ .  
 350 We employ a lag of  $\delta t = 5\text{min}$  between the interplanetary observations (which are prop-  
 351 agated from L1 to the bow shock) and  $\Phi_D$ , that being the lag derived by Lockwood and  
 352 McWilliams (2021b) between the hourly means of  $\Phi_{PC}$  and running hourly means of the  
 353 coupling function from IMF data when auroral electrojet activity was quiet ( $-AL \leq 100\text{nT}$ ).

354 A different analysis of the same dataset reveals that much of the scatter in Figure  
 355 1 is caused by a mechanism other than dayside magnetopause reconnection. Figure 2 shows  
 356 contours of observed transpolar voltage  $\Phi_{PC}$ , from the same dataset, as a function of hourly  
 357 means of the predicted lagged magnetopause reconnection voltage from Equation 5,  $\Phi_D$ ,  
 358 and the SuperMAG  $SML$  index. This index is constructed in the same way as the  $AL$   
 359 index but uses many more stations in the northern hemisphere (of order 100 instead of  
 360 the ring of 12) and so avoids the non-linear effect in  $AL$  caused by polar cap expansion

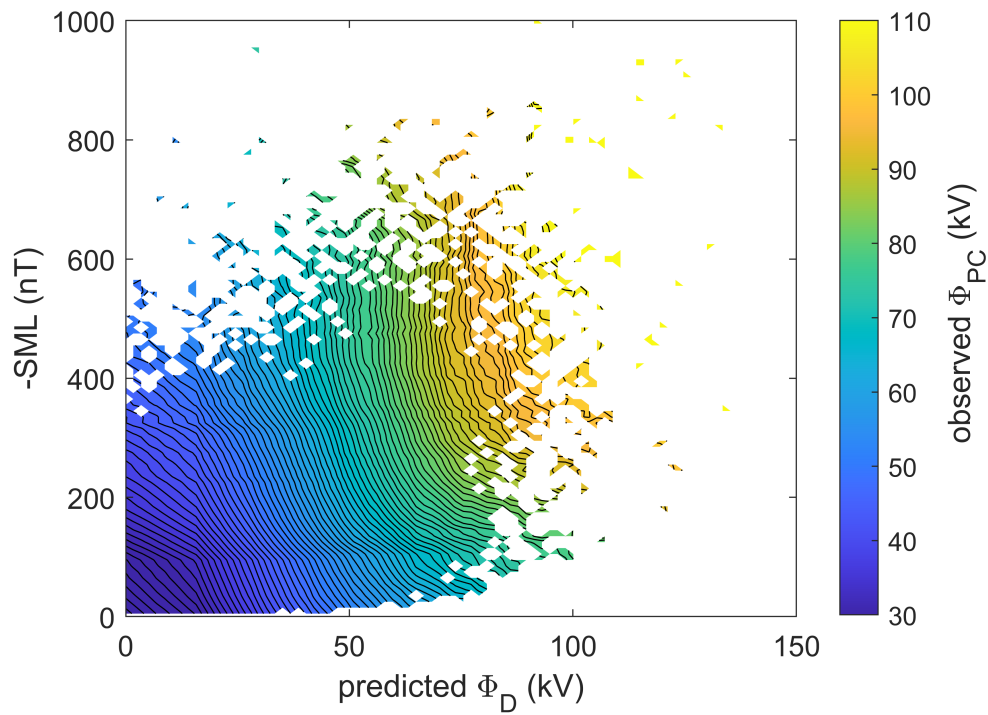


**Figure 2.** Contours of hourly means of transpolar voltage,  $\Phi_{PC}$ , as a function of the predicted magnetopause reconnection voltage from Equation 5,  $\Phi_D$ , and  $-SML$ . The observations are from the same survey of 25 years' data as Figure 1.

361 to equatorward of the ring of 12 stations (Gjerloev, 2012; Newell & Gjerloev, 2011). Be-  
 362 cause, like  $AL$ ,  $SML$  is increasingly negative with enhanced activity we here use  $-SML$   
 363 in plots and descriptions.

364 The key point to note about Figure 2 is that the contours slope diagonally across  
 365 the plot. This means that at a given predicted  $\Phi_D$  the transpolar voltage  $\Phi_{PC}$  increases  
 366 with increasing  $-SML$ . This is true in all regions of this parameter space except when both  
 367  $\Phi_D$  and  $-SML$  are very large when the contours become vertical showing that  $\Phi_{PC}$  is then  
 368 a function of  $\Phi_D$  only. Thus even using hourly data we can detect an influence on trans-  
 369 polar voltage which depends on the auroral electrojet activity level. This is therefore  
 370 a separate influence on the transpolar voltage, as predicted to be supplied by  $\Phi_N$  in the  
 371 ECPC model. The same picture emerges from the Active Magnetosphere and Planetary  
 372 Electrodynamics Response Experiment (AMPERE) analysis of data on field-aligned cur-  
 373 rents from magnetometers on board more than 70 Iridium satellites in circular low-Earth  
 374 orbit (altitude 780 km) in 6 orbit planes, which give 12 cuts at different MLTs in each  
 375 orbit through the auroral oval (Anderson et al., 2014; Milan et al., 2015): from Chree  
 376 analysis of these data, Milan et al. (2018) show that the field-aligned currents that bring  
 377 convection circulation of the magnetosphere down to the ionosphere are enhanced in re-  
 378 sponse both to a coupling function that quantifies dayside magnetopause reconnection  
 379 and also to the  $-AL$  index.

### 380 2.3 Determination of the reconnection voltage in the cross-tail current 381 sheet, $\Phi_N$

382 The problem in applying the ECPC is that the nightside reconnection voltage  $\Phi_N$   
 383 is hard to quantify (Walach et al., 2017; ye, 2018). Several studies have used Equation  
 384 1 to infer it from the rate of change of open polar cap flux  $dF_{PC}/dt$  and the value of  $\Phi_D$   
 385 deduced from interplanetary parameters using a coupling function of the type given by  
 386 Equation 5. For example, Grocott et al. (2002) used  $dF_{PC}/dt$  deduced from the bite-  
 387 out in the nightside polar cap in a substorm expansion phase observed by magnetome-  
 388 ters, radars and imagers. The same basis was used by Milan et al. (2007), ye (2018) and  
 389 Milan et al. (2021) using the circular polar cap assumption and looking at the change  
 390 in radius of the polar cap inferred from global auroral images or the locations of field-  
 391 aligned current sheets deduced from the AMPERE programme. This method is not use-  
 392 ful here where we wish to use  $\Phi_N$  to predict the variation of  $F_{PC}$ . The way forward was  
 393 first established by Holzer et al. (1986) who used the  $AL$  nightside auroral electrojet in-  
 394 dex as a proxy for  $\Phi_N$  to study two polar cap expansions and contractions using Equa-  
 395 tion 1. The validity of this approach has been confirmed by several studies of larger datasets,  
 396 including the statistical survey of 25 years of data by Lockwood and McWilliams (2021b)  
 397 who found that transpolar voltage was a function of  $\Phi_D$  with an independent influence  
 398 related to  $AL$ , something we have demonstrated here with Figure 2 using the SuperMAG  
 399  $SML$  index in place of  $AL$ . This confirms  $SML$  can be used as a basis for the quantifi-  
 400 cation of  $\Phi_N$ .

401 The mauve line in part (a) of Figure 3 is a polynomial fit to all the hourly means  
 402 of  $\Phi_{PC}$  from the survey of Lockwood and McWilliams (2021b) as a function of the si-  
 403 multaneous hourly means of  $-SML$ . There is considerable spread in the data which  
 404 we expect for two known reasons: firstly  $\Phi_D$  contributes to  $\Phi_{PC}$  as well as  $\Phi_N$ , and sec-  
 405 ondly there are ionospheric conductivity and other seasonal effects in the relationship  
 406 between  $\Phi_{PC}$  and the geomagnetic  $SML$  index. Part (b) of Figure 3 shows the equiv-  
 407 alent plot for strongly northward IMF ( $[B_Z]_{GSM} \geq 10nT$ ) when we can take  $\Phi_D$  to be  
 408 zero. The mauve line is the same as in part (a) and remains a good fit to the average  
 409 data, which covers a smaller range of both  $\Phi_{PC}$  and  $SML$ , as expected for northward IMF.  
 410 However, although the scatter is reduced because  $\Phi_D$  is not a factor, it is still consid-  
 411 erable.

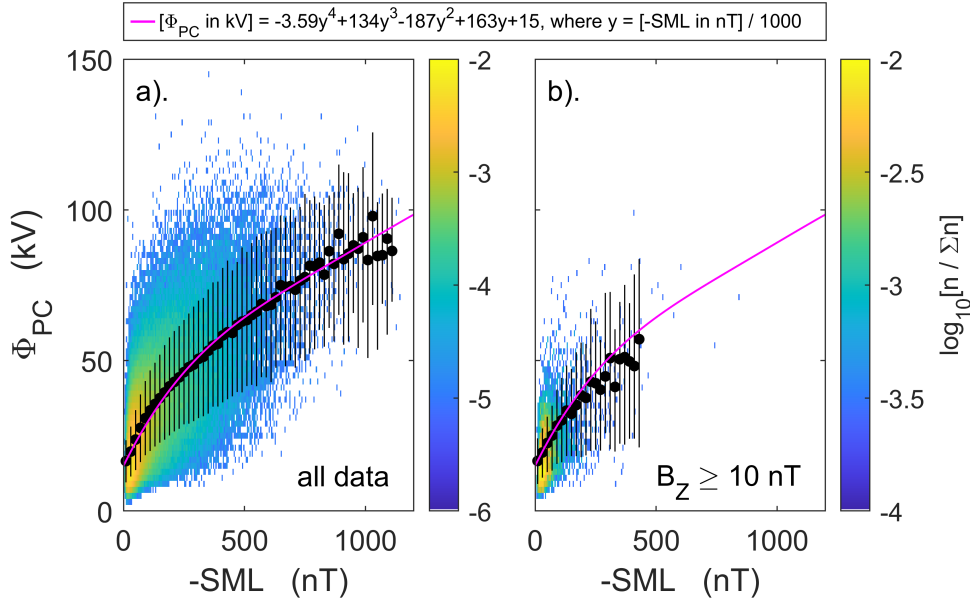


**Figure 3.** Scatter plots of observed hourly means of transpolar voltage,  $\Phi_{PC}$  as a function of  $-SML$ , where  $SML$  is the SuperMAG auroral electrojet index. The observations are from the survey of 25 years' data from the northern hemisphere coherent-scatter SuperDARN radar network by Lockwood and McWilliams (2021b). Both panels are for the full data set (1995–2019, inclusive); (a) is for all data and (b) for the subset of strongly northward IMF with  $B_Z \geq 10nT$ , lagged by the optimum delay between  $B_Z$  and  $\Phi_{PC}$  of  $\delta t = 18min$ . In both panels the fraction of valid samples,  $n/\Sigma n$ , is color-coded on a logarithmic scale as a function of observed  $SML$  and  $\Phi_{PC}$ , in bins of size  $5nT$  by  $2kV$ . As in Figure 1, only bins containing 3 or more samples are coloured. Also shown are the mean  $\Phi_{PC}$ , with error bars between the 15.9% and 84.1% of the cdf ( $1-\sigma$  points), for bins in  $SML$   $20nT$  wide in which there are 25 or more samples. The mauve lines in both panels is the best polynomial fit to the mean values in (a), given at the top of the Figure.

To estimate the contribution to  $\Phi_N$  of processes associated with the substorm current wedge, we adopt the fitted form to  $\Phi_{PC}$  as a function of  $SML$  (given at the top of Figure 2) but scale it with a factor  $k(F)$ , that is a function of time of year,  $F$ , to allow for the seasonal effects in these northern hemisphere radar and magnetometer data. This gives us an estimate of the tail reconnection rate associated with auroral electrojet activity, as quantified by  $SML$ :

$$[\Phi_{N1} \text{ in } kV] = k(F) \times f(SML) = k(F) \times [-3.59y^4 + 134y^3 - 187y^2 + 15] \quad (6)$$

where  $y = [-SML \text{ in nT}]$ .

However, the scatter in Figure 3b shows that  $SML$  does not uniquely define  $\Phi_N$ . The same conclusion can be drawn from the survey of 1-year of data by Milan et al. (2021) in which the ratio  $\Phi_N/SML$  appears to be different, on average, for different phases of magnetospheric behaviour. On the other hand, Milan et al. (2007) show that almost all  $\Phi_N$  occurs soon after bursts in  $\Phi_D$  and a base-level of  $\Phi_N$  between events was not detected. However, we note that the viscous-like voltage  $\Phi_V$  may well actually be due to low-level continuing  $\Phi_N$  because ongoing unbalanced nightside reconnection has the ability to mimic all the ionospheric flows that have been attributed to viscous-like interaction.

Compared to the the scatter in Figure 1, that in Figure 3 is large and so we here take steps to reduce it. Specifically, we add to the highly variable loss rate that is predicted by  $SML$  alone, which we term  $\Phi_{N1}$ , a second quasi-steady loss rate that depends only on the magnetic shear across the cross-tail current sheet (and hence related to the open flux  $F_{PC}$ ), but which does not register in  $SML$ : we call this second loss rate  $\Phi_{N2}$ , and is defined such that the total loss rate is

$$\Phi_N = \Phi_{N1} + \Phi_{N2} \quad (7)$$

We take this additional loss of  $F_{PC}$  to be linear with a time constant  $t_N$  so

$$\Phi_{N2} = F_{PC}(\delta t)/t_N \quad (8)$$

where  $\delta t$  is the lag to allow for the propagation of open flux into the tail after its generation (at rate  $\Phi_D$ ). We here use  $\delta t = 15 \text{ min.}$ , the derived optimum lag between the predicted  $\Phi_D$  and observed  $\Phi_{PC}$  in the study by (Lockwood & McWilliams, 2021b, -see their Figure 6). We repeated our analysis for  $\delta t = 10 \text{ min}$  and  $\delta t = 30 \text{ min}$  and found only small changes to our results. Note that there is a potential improvement we could make to Equation 8 in that the rate could be made a function of solar wind dynamic pressure  $p_{SW}$  and the dipole tilt angle  $\delta$  as there are observations that indicate that, together, they influence the rate of nightside reconnection by squeezing the tail (Schieldge & Siscoe, 1970; Caan et al., 1973; Kokubun et al., 1977; Karlsson et al., 2000; Finch et al., 2008; Hubert et al., 2009; Yue et al., 2010; Lockwood, 2013; Lockwood, McWilliams, et al., 2020; Lockwood, Owens, Barnard, Watt, et al., 2020; Lockwood et al., 2021). This would not influence the equation for the voltage  $\Phi_{N1}$  as any raise in  $-SML$  is accounted for; however, it could influence  $\Phi_{N2}$  if  $\Phi_N$  were increased by more than is predicted from the rise in  $-SML$ . However, variations in  $p_{SW}$  have also been proposed to influence  $\Phi_D$ , field aligned currents and Joule heating (Lukianova, 2003; Lee, 2004; Palmroth, 2004; Boudouridis, 2005; Stauning & Troshichev, 2008): hence, it might be possible to include solar wind dynamic pressure effects in one area and not another. To be sure that we are not inconsistent in the present paper we do not include the effects of  $p_{SW}$  variations in

453 the present analysis. However, we do highlight times when changes in  $p_{SW}$  may have had  
454 an effect.

455 The reason for proposing a second component of  $\Phi_N$  that does not depend on  $SML$   
456 is that without it we found that during the events studied  $F_{PC}$  grows to either unreal-  
457 istic values (exceeding  $2.5GWb$ ) and/or falls to below zero for any  $k(F)$ . This is because  
458 in the delays between enhanced  $\Phi_D$  and the  $SML$  response, positive  $(\Phi_D - \Phi_N)$  can be  
459 very large if  $\Phi_N$  is only based on  $SML$  and so  $F_{PC}$  can grow unrealistically large. Con-  
460 versely there are intervals when  $\Phi_D$  has declined (i.e., the IMF has turned northward)  
461 but  $SML$  remains high and these can give large negative  $(\Phi_D - \Phi_N)$  and if they per-  
462 sist for long enough the estimated  $F_{PC}$  turns negative, which is unphysical. We found  
463 that, for the event studied here, quantifying  $\Phi_N$  from  $SML$  alone, there was no scaling  
464 factor which could prevent  $F_{PC}$ , at certain times, becoming negative and from ever be-  
465 coming unrealistically large (and in fact, usually both occurred).

466 To compute the scaling factor  $k(F)$ , for the time of year  $F$  of the events (early Febru-  
467 ary) we make use of the fact that averaged over a long enough period  $\tau$ , the means  $\langle \Phi_D \rangle_\tau$   
468 and  $\langle \Phi_N \rangle_\tau$  become equal and hence steady-state applies (and by Equation 2, the polar  
469 cap flux is constant). Choosing the interval  $\tau$  needed, however, is a compromise between  
470 two factors: if  $\tau$  is too large the seasonal variation between  $\Phi_N$  and  $SML$  becomes a fac-  
471 tor but if it is too short (less than a couple of days) then steady-state is not achieved.

472 In order to find an interval around the events of interest we searched for two times  
473 that were of order one week apart for which both the predicted  $\Phi_D$  (from Equation 1)  
474 and observed  $-SML$  were very low (below  $1kV$  and  $20nT$ , respectively) and followed in-  
475 tervals of at least 1 day when  $\Phi_D$  and  $-SML$  had remained low. Two such times around  
476 the events of interest were  $UT = 11$  hrs of day-of-year (d-o-y) 30 (30 January, 2022) and  
477  $UT = 5$  hrs on d-o-y 38 (7 February, 2022), giving an interval of duration  $\tau$  of 7.75 days.  
478 At these times, images of the auroral oval (see below) gave similar and small values of  
479  $F_{PC}$  of  $0.267 \pm 0.014GWb$ . Therefore the difference  $\Delta F_{PC} = 0 \pm 0.028GWb$  and the un-  
480 certainty in  $\Delta F_{PC}/\Delta t = \Delta F_{PC}/\tau$  is  $41.8Wbs^{-1}$ , in other words  $0.042kV$ . This is the  
481 level to which the averages of  $\Phi_D$  and  $\Phi_N$  can be taken as equal for this interval. We  
482 will refer to this as the ‘‘calibration interval’’. From Equations 1, 6, 7 and 8

$$dF_{PC}/dt = \Phi_D - k(F) \times f(SML) - F_{PC}(\delta t)/\tau_N \quad (9)$$

483 Equation 9 has two unknowns,  $k(F)$  and  $\tau_N$  - but for given values of these two pa-  
484 rameters we can compute the variation of  $F_{PC}$  from the known variations of  $\Phi_D$  and  $SML$ .  
485 We start these computations for a wide range of initial values of  $F_{PC}$  at the start of doy  
486 1 of 2022 and we find that this initial condition has no effect on the variation after d-  
487 o-y 30 (January 30, 2022). For a given  $\tau_N$ , we iterate  $k(F)$  until  $F_{PC}$  at the end of the  
488 calibration interval equals that its start. This means that the integral of  $\Phi_D$  over the in-  
489 terval equals the integral of  $\Phi_N$  and steady state is achieved over this timescale.

490 If  $\tau_N$  is too small  $F_{PC}$  becomes negative. If  $\tau_N$  is too large we find  $F_{PC}$  reaches  
491 peaks larger than the largest values that have been detected, which are near  $1GWb$  (Boakes  
492 et al., 2009; Milan et al., 2021). We find that this  $F_{PC}$  is reached in both the peaks in  
493 the event studied here for  $\tau_N = 6.8min$ . Section 4 provides evidence that it is an ap-  
494 propriate value for  $\tau_N$ .

#### 495 2.4 Universal Time effect: polar cap motions

496 A series of 4 papers Lockwood, Owens, Barnard, Haines, et al. (2020); Lockwood,  
497 McWilliams, et al. (2020); Lockwood, Owens, Barnard, Watt, et al. (2020); Lockwood  
498 et al. (2021) have investigated the semi-annual and Universal Time (UT) variations in  
499 the magnetosphere and in geomagnetic activity. The last of this series brings the con-

500 clusions together and successfully models the  $UT$  (and annual) variations of observed  
 501 hemispheric geomagnetic indices by introducing a key component that had been hith-  
 502 erto overlooked. The interplanetary electric field is measured by spacecraft in geocentric-  
 503 solar frames, such as GSM, GSE or GSEQ, i.e. frames that are fixed in relation to the  
 504 centre of the Earth with an X-axis between the centres of the Earth and the Sun. Be-  
 505 cause Earth's magnetic poles are offset from the rotational poles, the magnetic poles and  
 506 the ionospheric polar caps move in the GSE and GSEQ frames in a diurnal circle gener-  
 507 ating almost circular loci (Lockwood et al., 2021). For GSM (for an eccentric dipole  
 508 field but the GSE-to-GSM rotation angle determined using a geocentric dipole), the mo-  
 509 tions are ellipses but with the major axis in the X-direction of length equal to the di-  
 510 ameter in the same direction of the loci for GSEQ and GSE. In this paper we are con-  
 511 cerned with the component of motion in the X-direction which is the same for GSE, GSEQ  
 512 and GSM frames.

513 Figure 4 illustrates these pole motions. Note that, by convention, the north/south  
 514 pole of a magnet is where field lines diverge/converge and so, for the current polarity of  
 515 the geomagnetic field, the magnetic pole in the southern hemisphere is, by that conven-  
 516 tion, a 'north' magnetic pole and *vice-versa*: in this paper, we refer to a magnetic pole  
 517 by the hemisphere of the Earth that it is in and not by the magnet convention. At around  
 518 05hrs  $UT$  the north magnetic pole (i.e. the magnetic pole in the northern hemisphere)  
 519 is pointed away from the Sun and the south magnetic field is pointed toward it, as shown  
 520 in Figure 4a. At around 17hrs  $UT$  the north/south magnetic pole is pointed toward/away  
 521 from the Sun (Figure 4c). Between these two times, around 11hrs  $UT$  the north/south  
 522 magnetic pole is moving toward/away from the Sun (Figure 4b) and at around 23hrs  $UT$   
 523 the north/south magnetic pole is moving away from/toward the Sun (Figure 4d). The  
 524 sunward component of the motion of the north/south magnetic pole at ionospheric F-  
 525 region altitudes in any geocentric-solar frame is  $V_{NP}$  and  $V_{SP}$ , respectively. These mo-  
 526 tions can be seen in the right-hand panels which show the pole loci at an altitude of 800  
 527 km with a dot denoting where the pole is at the  $UT$  in question. The sunward/antisunward  
 528 velocities of the poles in the GSEQ frame are almost independent of the time-of-year and  
 529 the larger offset of the pole in the Southern hemisphere from the rotational axis makes  
 530 the radius of the near-circular orbits roughly twice as large as in the north and so the  
 531 amplitude of the diurnal variation in  $V_{SP}$  is roughly twice that in  $V_{NP}$ . Note also that  
 532 the longitude separation for the eccentric field poles is smaller than the  $180^\circ$  that it would  
 533 be for a geocentric field and so the variations in  $V_{SP}$  and  $V_{NP}$  are not in exact antiphase.

534 Both global images (Stubbs et al., 2005) and geomagnetic field modelling (Tsyganenko,  
 535 2019) of the auroral oval show that the polar cap moves with its magnetic pole with very  
 536 little change in shape. There are a number of observations relevant to these diurnal mo-  
 537 tions of the polar cap caused by Earth dipole tilt. Newell and Meng (1989) surveyed 3  
 538 years' data from the DMSP (Defense Meteorological Satellite Program) F7 satellite and  
 539 showed that the region of solar wind precipitation in the cusp region migrated in geo-  
 540 magnetic latitude by about  $0.06^\circ$  for each  $1^\circ$  shift in dipole tilt angle. That means that  
 541 (94%) of the motion of the magnetic pole in a geocentric-solar frame is reflected in the  
 542 cusp location and only 6% in the geomagnetic frame. The key point is that the cusp bound-  
 543 ary and the magnetic pole location are defined in the same geomagnetic latitude frame  
 544 and the fact that their separation changes very little, means that their separation also  
 545 changes very little when both are transformed into a geocentric-solar frame, no matter  
 546 what geomagnetic latitude frame was used to measure their separation. The cusp pre-  
 547 cipitation is on newly-opened field lines generated by the voltage  $\Phi_D$  (see review by Smith  
 548 & Lockwood, 1996) and hence this dipole-tilt induced motion of the dayside open-closed  
 549 boundary (OCB) in a geocentric-solar frame mainly reflects that in the magnetic pole.  
 550 Similarly on the nightside, Vorobjev and Yagodkina (2010) showed that the magnetic  
 551 latitude of the poleward edge of the nightside northern-hemisphere auroral oval, as de-  
 552 tected in DMSP satellite data from 1986, had a sinusoidal diurnal variation in ampli-  
 553 tude near  $2^\circ$ , whereas the offset of the rotational northern eccentric axial pole at that

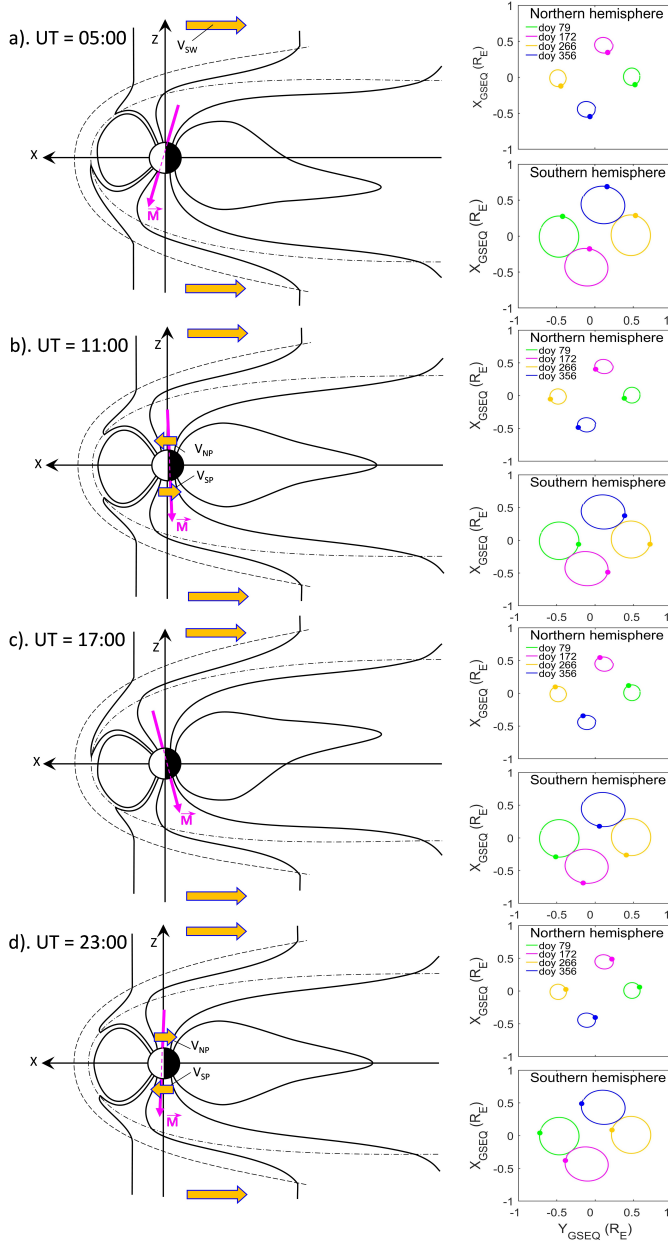


**Figure 4.** The left-hand column gives schematics of pole motions in a geocentric frame, based on the global MHD model predictions in Lockwood, Owens, Barnard, Watt, et al. (2020). The right hand panels show the loci of the axial poles, at an altitude of  $800\text{km}$  and over 24 hours, in the geocentric-solar GSEQ frame, predicted using the eccentric dipole model of Koochak and Fraser-Smith (2017) for the year 2018. The schematics show the magnetosphere in the noon-midnight (GSEQ XZ) plane at (a)  $05\text{hrs UT}$ ; (b)  $11\text{hrs UT}$ ; (c)  $17\text{hrs UT}$ ; and (d)  $23\text{hrs UT}$  at equinox. The mauve arrow shows the magnetic moment of an eccentric dipole. The dot-dashed lines are the magnetopause and the dashed lines the bow shock. Outside the bow shock the solar wind flows in the  $-X$  direction at speed  $V_{SW}$ . The pairs of panels in the right hand column give the pole loci in the GSEQ frame for the northern and southern hemispheres and four times of year: (green) March equinox, (mauve) June solstice, (orange) September equinox and (blue) December solstice. The coloured dots on each locus shows the pole position at the  $UT$  of the corresponding schematic on the left-hand side.

554 time was about  $8^\circ$ . Hence in a geocentric-solar frame only about 75% the motion in the  
 555 magnetic pole is reflected in this boundary. However, this boundary is generally equa-  
 556 torward of the nightside OCB and this is likely to make this percentage a poor estimate  
 557 of the real value that would apply to the nightside OCB. The magnetic field tracing needed  
 558 by global MHD model of the magnetosphere means that the OCB can be identified in  
 559 simulations and Kabin et al. (2004) found that magnetic latitude shifts in the noon OCB  
 560 were  $1.3^\circ$  and  $-0.9^\circ$  for dipole tilts of  $+35^\circ$  and  $-35^\circ$ , i.e., 3.9% and 2.7%, respectively.  
 561 The corresponding shifts in the midnight OCB were  $0.8^\circ$  and  $-0.5^\circ$  (2.3% and 1.5%, re-  
 562 spectively). Hence these simulations show the nightside OCB moves even more closely  
 563 with the magnetic pole than the dayside OCB. The fact that the OCB is largely mov-  
 564 ing with the geomagnetic poles shows that closed field lines outside the open field line  
 565 region are also taking part in this diurnal wobble caused by the pole motion. Oznovich  
 566 et al. (1993) showed that during low auroral activity, the auroral oval as a whole was  
 567 shifted by  $1^\circ$  in geomagnetic coordinates for every  $10^\circ$  change in the dipole tilt angle (90%).  
 568 Being at large longitudinal separations (if not exactly the  $180^\circ$  for a geocentric dipole  
 569 model) the motion of the auroral ovals induced by the magnetic pole motions would be  
 570 close to, but not exactly, in antiphase in a geocentric-solar frame with the southern pole  
 571 moving antisunward when the northern is moving sunward, and *vice-versa*. This was di-  
 572 rectly observed by (Stubbs et al., 2005), using full and simultaneous auroral images of  
 573 the northern and southern auroral ovals made by the IMAGE and Polar satellites.

574 In the northern hemisphere the sunward speed of motion  $V_{NP}$  is a sine wave of am-  
 575 plitude  $57ms^{-1}$ , but the larger offset of the southern magnetic pole from the rotational  
 576 pole makes the corresponding amplitude of the speeds there,  $V_{SP}$  about  $135ms^{-1}$ . These  
 577 values were computed using the the eccentric dipole field model of the geomagnetic field  
 578 by Koochak and FraserSmith (2017) by Lockwood et al. (2021). This eccentric dipole  
 579 model uses the first 8 Gauss coefficients of the IGRF model that define a spherical har-  
 580 monic expansion of the magnetic scalar potential; this is compared to the first three used  
 581 to define a centred dipole. This is a standard way of describing an eccentric dipole (Bartels,  
 582 1936). The speeds of these motions of the polar cap in a geocentric-solar frame are very  
 583 much smaller than that of the solar wind. However, in the ionosphere the magnetic field  
 584  $B_i$  is approximately  $5 \times 10^{-5}T$ , which is much greater than the flow-perpendicular field  
 585 in interplanetary space (which is typically  $5nT$ ). The diurnal motion toward and away  
 586 from the Sun induces an electric field across the northern polar cap in a geocentric-solar  
 587 frame of  $V_{NP}B_i$  and a voltage in that frame across the polar cap of  $\phi_{MN} = V_{NP}B_i d_{PC}$ ,  
 588 where  $d_{PC}$  is the polar cap diameter. Using a typical polar cap angular radius of  $15^\circ$  gives  
 589  $d_{PC} \approx 3.6 \times 10^6 m$  and a sinusoidal diurnal voltage variation of amplitude  $10kV$ . In the south-  
 590 ern hemisphere, the larger offset of the poles means that this amplitude is  $24kV$ . An-  
 591 other important factor is that the the pole-motion voltages are applied consistently, ris-  
 592 ing and falling again sinusoidally over a 12-hour period, whereas rapid variations on IMF  
 593 orientation mean that the voltages associated with solar wind flow are only consistently  
 594 applied over intervals of several hours during rare, large CME events. Note also the im-  
 595 portance here of the eccentric dipole model. Use of a geocentric dipole makes every ef-  
 596 fect on the north pole motion equal and opposite to that of the south pole. Hence for  
 597 a geocentric dipole, although Earth's rotation alternately causes a given effect in one hemi-  
 598 sphere and then the other, the global effect (the sum of the two) is always zero. This is  
 599 not the case for an eccentric dipole.

600 These effects of pole motions, like the conductivity-induced changes discussed ear-  
 601 lier, change the balance between directly-deposited energy and energy stored in the tail  
 602 and then deposited via the storage-release system. Let us consider the Northern polar  
 603 cap: when it is moving sunward (with a velocity  $V_{NP} > 0$  that peaks at around 12 UT)  
 604 the antisunward convection in the polar cap in a geocentric-solar frame will be reduced  
 605 by the motion of the cap as a whole (i.e. by  $V_{NP}$ ) and the voltage across the cap in that  
 606 frame will be reduced by  $\phi_{MN} = V_{NP}B_i d_{PC}$ , even if the reconnection voltages  $\Phi_D$  and  
 607  $\Phi_N$  are unchanged. The convection pattern perturbations for sunward/antisunward mo-

tions of the polar cap as a whole (and dawnward/duskward motions) were sketched by (Lockwood, 1991). This means the directly-deposited Joule heating is reduced. In a geocentric-solar frame, the flux transfer rate over the northern ionospheric polar cap is reduced to  $\Phi_{PC} - \phi_{MN}$  but, given that the voltage across the region of open field lines in interplanetary space is unchanged, this means that flux is accumulating in the northern lobe at a rate that is  $\phi_{MN}$  greater than it would have done if  $V_{NP}$  had been zero. Conversely, in the other 12-hour phase of the diurnal cycle the transpolar voltage is enhanced because  $V_{NP}$  and  $\phi_{MN}$  are negative and the rate of flux storage in the tail lobe is reduced. Hence the transpolar voltage in the northern polar cap is

$$\Phi'_{NC} = \Phi_{PC} - \phi_{MN} = \Phi_{PC} - V_{NP}B_i d_{PC} \quad (10)$$

and in the southern hemisphere

$$\Phi'_{SC} = \Phi_{PC} - \phi_{MS} = \Phi_{PC} - V_{SP}B_i d_{PC} \quad (11)$$

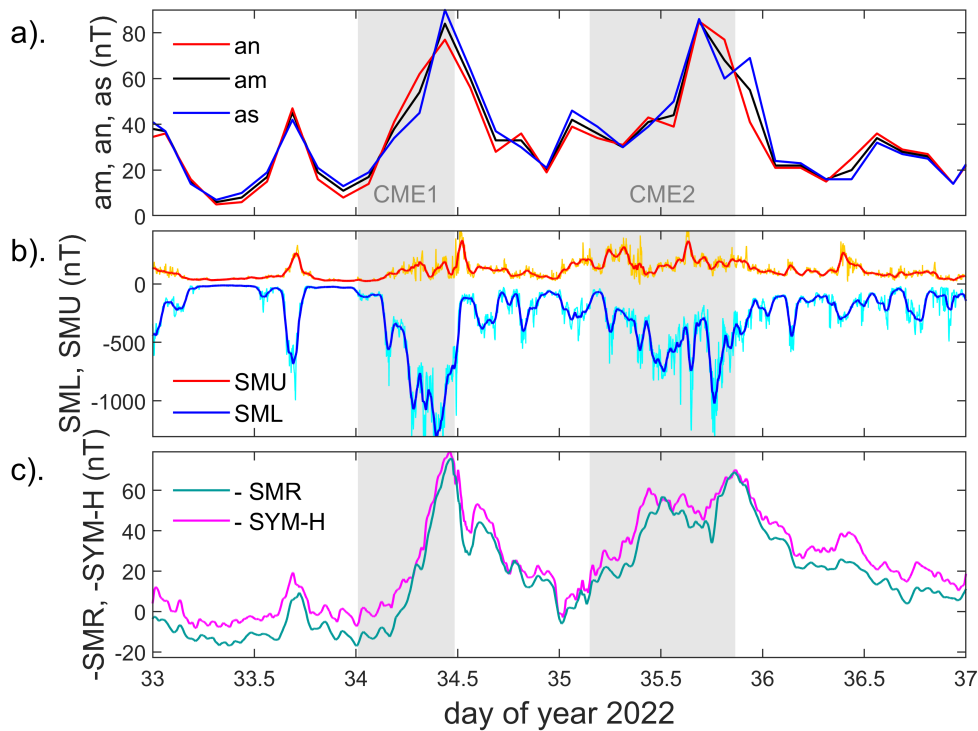
where  $V_{NP}$  and  $V_{SP}$  are the sunward components of motion of the northern and southern polar caps.

If the variations of  $V_{NP}$  and  $V_{SP}$  were of the same amplitude and in antiphase then although there would be more power deposited in the northern polar cap (and less stored in the northern tail lobe) for half the day, and then more in the southern hemisphere (and less stored in the southern tail lobe) for the other half so that the sum of the two would be constant. However these motions are not of equal amplitude, nor are they exactly in antiphase and this leaves a net  $UT$  variation in power deposited (and that stored in that tail) globally (Lockwood et al., 2021).

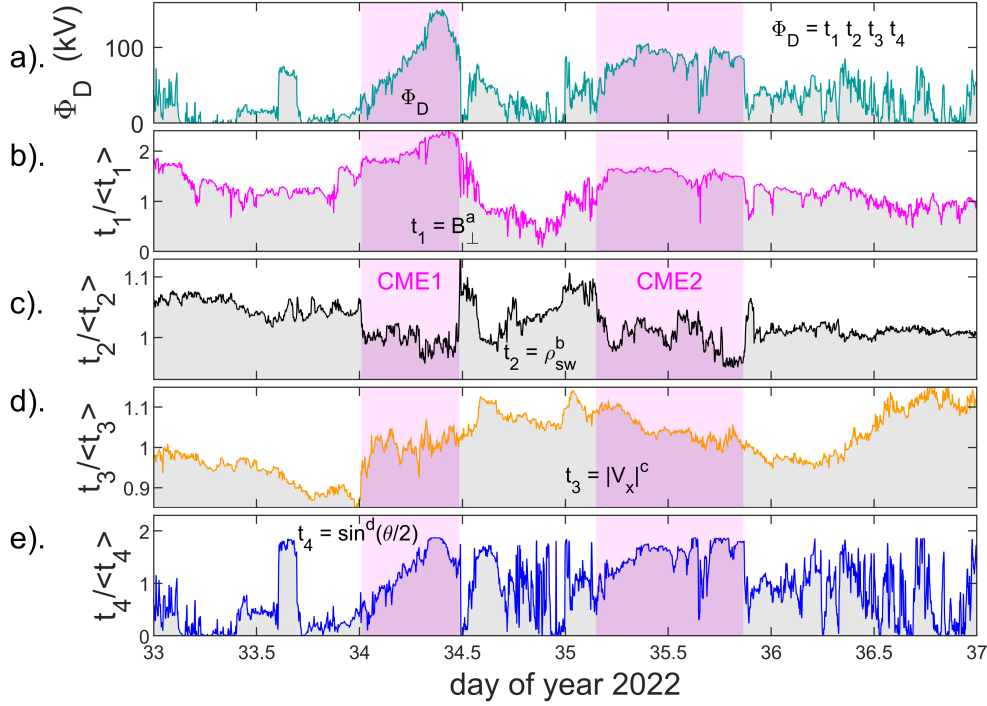
Note that the voltage imposed by the solar wind flow,  $\Phi_{PC}$ , across the polar caps of the two hemispheres can be different at any one instant of time because of different inductive changes in the magnetic fields of the two tail lobes. However, on average they must be the same: by Faraday's law, a voltage is synonymous with a magnetic flux transfer rate and maintaining  $\nabla \cdot \mathbf{B} = 0$  means that the long-term average of flux transport over the south pole must equal that over the north pole. In other words  $\langle \Phi_{PC} \rangle$  must be the same in the two hemispheres on average. A number of statistical studies of satellite data report differences in the long-term averages of the transpolar voltage in the two hemispheres (e.g., Frster & Haaland, 2015) which almost certainly reflect aliasing of orbit paths with seasonal,  $UT$  and activity level variations and not a violation of  $\nabla \cdot \mathbf{B} = 0$ .

### 3 The event of 3-4 February 2022

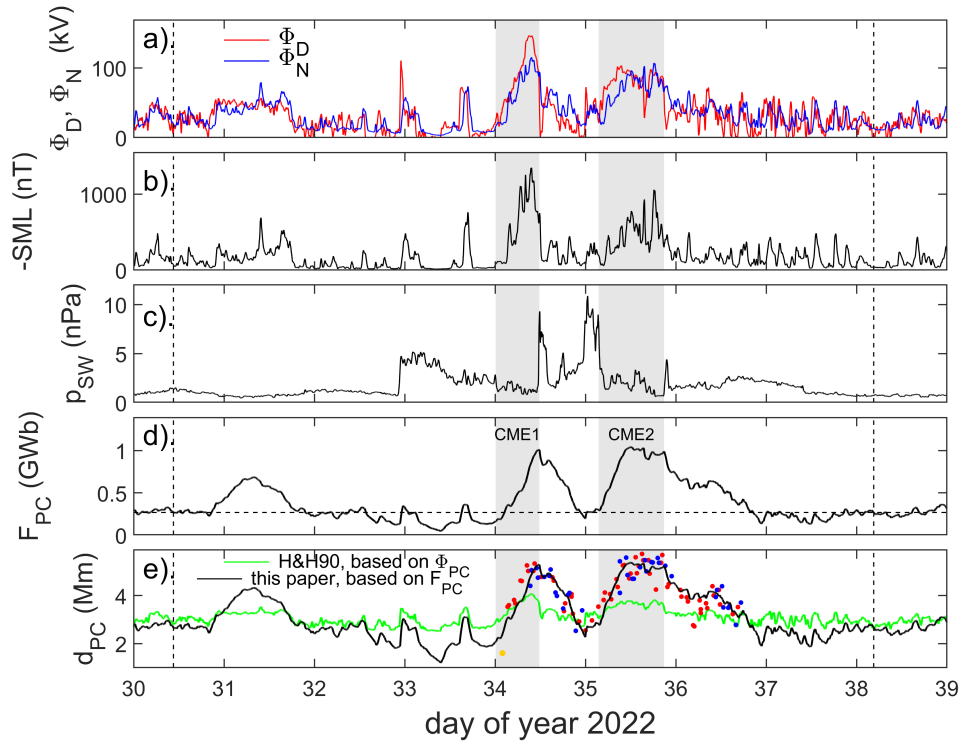
Figure 5 shows the variations of various geomagnetic activity indices during the events of early February 2022. The gray bands mark the times of the CME passages past the Earth, as defined from interplanetary data by Dang et al. (2022). The top panels show the 3-hourly planetary range indices,  $am$ ,  $an$ , and  $as$  with peaks near the ends of each of the CME events. Both peaks reach  $86nT$  in the global  $am$  index. The variations of the hemispheric sub-indices,  $an$ , and  $as$ , are very similar to that for  $am$ . Panel (b) shows large enhancements in the nightside auroral electrojet index  $-SML$  at the times of the peaks in  $am$ . The bottom panel shows the  $SMR$  and  $SYM-H$  indices compiled from low-latitude stations and mainly responding to the ring current. These show intensifications that peak shortly after the peaks in  $-SML$  but which decay more slowly. Note the data in panels (b) and (c) have been smoothed with 20-minute running (boxcar) means to reveal the variations on timescales that can be compared to the  $am$  index and below are compared to satellite observations of the polar cap which are available, on average, about every 40 minutes.



**Figure 5.** Geomagnetic indices during the events of 3-4 February 2022. Plots are for 00 UT on 2 February (d-o-y 33) to 00UT on 6 February (d-o-y 37). The grey bands mark the times of the passages of the two CME events at Earth's bow shock, as identified by Dang et al. (2022). (a). The mid-latitude range  $am$  index (in black) with its northern and southern hemisphere components,  $an$  (in red) and  $as$  (in blue). (b). The SuperMAG SMU (red/orange) and SML (blue/cyan) auroral electrojet indices: the orange and cyan lines are the 1min values and the red and blue lines are 20min running means of those 1-min. data (c). 20min running means of the  $SMR$  and  $SYM-H$  indices. .



**Figure 6.** Variations of 1-minute integrations of solar wind parameters during the interval shown in Figure 5. Panel (a) shows the derived magnetopause reconnection voltage  $\Phi_D$ , given by Equation 5, and the panels beneath show the component terms, normalised to their mean value in the interval. (b).  $t_1 = B_{\perp}^a$  where  $B_{\perp} = (B_Y^2 + B_Z^2)^{1/2}$  is the IMF transverse to the  $X$  direction of the Geocentric Solar Magnetospheric (GSM) frame in which the  $Y$  and  $Z$  components are  $B_Y$  and  $B_Z$ . (c).  $t_2 = \rho_{sw}^b$  where  $\rho_{sw}$  is the solar wind mass density. (d).  $t_3 = |V_x|^c$  where  $V_{sw}$  is the  $X$ -component of the solar wind velocity. (e).  $t_4 = \sin^d(\theta/2)$  where  $\theta = \tan^{-1}(|B_Y|/|B_Z|)$  is the IMF clock angle in the GSM frame. The best-fit exponents are  $a = 0.6554$ ,  $b = 0.0522$ ,  $c = 0.6676$ ,  $d = 2.5$ . The vertical pink bands show the times of the CME passages. All parameters are lagged by the inferred propagation time to the dayside ionosphere of  $\delta t = 5 \text{ min}$ .



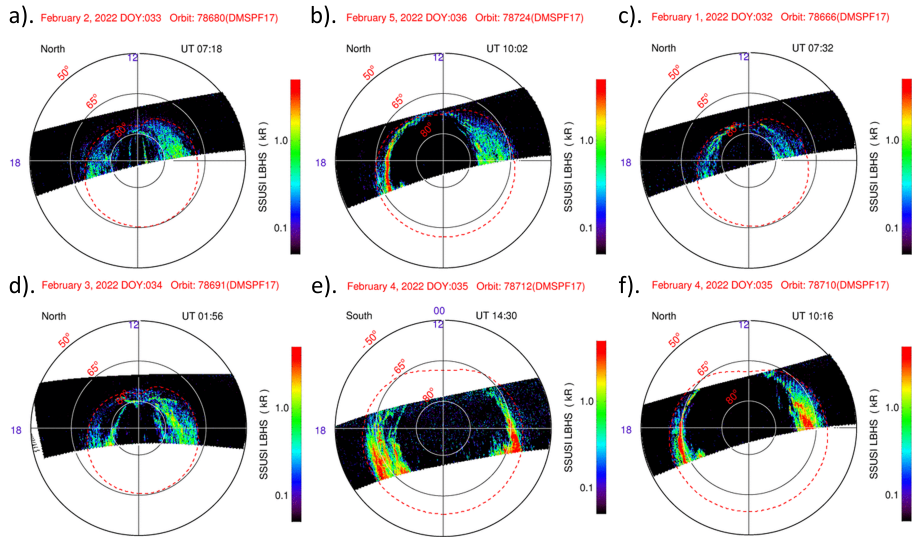
**Figure 7.** Modelled variations of polar cap voltages, flux and diameter. The vertical dashed lines delineate the “calibration interval” defined in the text. (a) the dayside magnetopause reconnection voltage ( $\Phi_D$ , in red) and the nightside tail current sheet voltage ( $\Phi_N$ , in blue). (b).  $-SML$  (c). the solar wind dynamic pressure,  $p_{SW}$  (d). The open polar cap flux,  $F_{PC}$ . (e). The polar cap diameter  $d_{PC}$  (black line) derived from  $F_{PC}$  using interpolation of the variation defined by Equation 3 and (green line) derived from  $\Phi_{PC}$  using the fit presented by Hairston and Heelis (1990) (H&H90). The modelling uses  $\tau_N = 6.81min$  (see text for details). The red and blue dots show dawn-dusk polar cap diameters taken from images by the Special Sensor Ultraviolet Spectrographic Imagers (SSUSI) instruments on board the Defense Meteorological Satellite Program (DMSP) F-17 and F-18 satellites. (see Figure 8),

Figure 6a gives the predicted dayside reconnection voltage  $\Phi_D$  computed from the interplanetary measurements: the other panels give the normalised variations of the terms from which it is computed. It can be seen that the mass density in each CME was slightly depressed and the transverse component of the IMF was enhanced, particularly during the first CME. The solar wind speed factor varied by about  $\pm 10\%$  in the interval: it was increased by the passage of CME1 but fell during CME2 and rose again roughly 12 hours after it had passed. Figure 6d shows that the IMF swings to strongly southward towards the end of the first CME passage and during much of the second CME passage, giving higher  $\Phi_D$  at these times. The first CME gives a particularly large peak in  $\Phi_D$  near its trailing edge, reaching  $150kV$  and exceeding  $85kV$  for  $5.7hr$  (6.1 to 11.8 hr UT on d-o-y 34). The second CME gives are more sustained period of somewhat smaller magnetopause reconnection voltage, being between  $85kV$  and  $103kV$  for most of an interval of duration  $11.3hr$  (9.4 to 20.7 hr UT on d-o-y 35).

#### 4 Analysis of polar cap behaviour during the event

Part (a) of Figure 7 shows the variation of  $\Phi_D$  computed using Equation 5 in red. In blue is the estimated variation of  $\Phi_N$ , computed from the observed *SML* index variation, shown in part (b), using Equations 6, 7 and 8. Part (d) shows the variation in open flux  $F_{PC}$  derived using equation 9. These variations use the optimum combination of  $\tau_N = 6.81min$  and  $k(F) = 0.9972$ . It was found that  $\tau_N \leq 5.33min$  gave times when  $F_{PC}$  became negative during the calibration interval and that  $\tau_N \geq 10.52min$  gave times when  $F_{PC}$  exceeded  $1.2GWb$ , which is larger than the values reported in the literature and than a proposed upper limit for a saturated polar cap. Substorm onsets are typically initiated when  $F_{PC}$  reaches about  $0.9GWb$  (Milan et al., 2008). Indeed, Boakes et al. (2009) find that the probability of a substorm onset occurring is zero for  $F_{PC}$  below about  $0.3GWb$  and increases linearly with  $F_{PC}$  at higher values to near unity at  $0.9GWb$ , but the numbers of available events in their study mean the probability at and above this open flux are not well defined. However, larger values of  $F_{PC}$ , up to about  $1.1GWb$ , have been deduced in sawtooth events and steady convection events (DeJong et al., 2007; Lockwood et al., 2009; Brambles et al., 2013). It has been estimated that in large superstorms,  $F_{PC}$  effectively saturates at  $1.2GWb$  (Mishin & Karavaev, 2017). In order to set the value of  $\tau_N$  within this allowed range, we look at the modelled diameter of the polar cap in the calibration interval, as this a strong function of  $\tau_N$ . The black line in Part (e) shows the variation in  $d_{PC}$  for the variation of  $F_{PC}$  shown in Part (d). This is obtained by PCHIP (Piecewise Cubic Hermite Interpolation Polynomial) interpolation of the variation of  $F_{PC}$  with  $d_{PC}$  given by Equation 3. PCHIP was used because it gives a monotonic variation without the erroneous overshoot that many splines can generate (it is continuous in both value and first derivative). Like linear interpolation, PCHIP ensures that the fitted polynomial passes through the data points and to check values between points are sensible, the analysis was repeated using linear interpolation and the results were not radically different. The green line in Figure 7d is from an empirical fit to DMSP ionospheric convection data given in Figure 5 of Hairston and Heelis (1990) (H&H90) which yields  $d_{PC}$  as a function of transpolar voltage  $\Phi_{PC}$  and which is here evaluated from  $\Phi_D$ ,  $\Phi_N$  and  $\Phi_V$ , using Equation 2. It can be seen that the variation of the two estimates of  $d_{PC}$  have similarities, but that the empirical model shows less variation than the one derived here. Figure 5 of H&H90 shows considerable scatter about the fitted line and so this difference is not unexpected. It is also worth noting that the average variation deduced from that plot is quite similar to the variation derived theoretically by Siscoe (1982). The value of  $\tau_N = 6.81min$  adopted here makes the averages of these two variations the same over the calibration interval. It yields an open flux  $F_{PC} = 0.26GWb$  at the start and end of the calibration interval, which is lower than the average value near  $0.4GWb$  in the surveys by Boakes et al. (2009) and Milan et al. (2021). It also yields peak values of  $1.01GWb$  at the end of CME1 and  $1.03GWb$  at the end of CME2. Valuable confirmation of the value of  $\tau_N$  comes from images of the northern and southern auroral ovals by the Special Sensor Ultraviolet Spectrographic Imager (SSUSI) on board the Defense Meteorological Satellite Program (DMSP) F-17 and F-18 satellites (Paxton et al., 2002, 2021). These images are in the Lyman-Birge Hopfield (LBH) short band (LBHS, 140–160 nm) of molecular nitrogen and the observed swathes usually show the full extent dawn-dusk diameter of the dark region poleward of the auroral oval. The poleward edge of the aurora seen in Far Ultraviolet (FUV) is often used as a proxy indicator of the OCB (Longden et al., 2010) and the six DMSP/SSUSU FUV images presented in Figure 2 of Y. Zhang et al. (2022) for the period studied here indicate considerable variability of the polar cap diameter.

In general, there is a difference between the latitude of the OCB, as identified in particle precipitation data and the poleward edge of the aurora, giving a dark ring of closed field lines poleward of the poleward edge of the aurora. The latitudinal width of this offset,  $\delta\Lambda$  will, to some extent, depend on the imager, the magnetic local time (MLT) and the intensity of the auroral precipitation. Carbary et al. (2003) found that  $\delta\Lambda$  did vary



**Figure 8.** Selected sample auroral images recorded by the Special Sensor Ultraviolet Spectrographic Imagers (SSUSI) instruments on board the Defense Meteorological Satellite Program (DMSP) F-17 and F-18 satellites in the Lyman-Birge Hopfield (LBH) short wavelength band (LBHS, 140–160 nm). See text for details.

systematically with MLT but argued a constant value of  $3.5^\circ$  could be used for the purposes of computing  $F_{PC}$ . Boakes et al. (2008) found  $\delta\Lambda \leq 1^\circ$ , except in the predawn and evening sectors, where values up to  $2^\circ$  may apply. Longden et al. (2010) find that near dawn and dusk, the sectors of interest here,  $\delta\Lambda \approx 1^\circ$  applies and that is what we adopt here.

There is an interesting minimum in the modelled  $F_{PC}$  at  $UT$  of  $9.5hrs$  on d-o-y 33 which is as low as  $0.05GWb$ . This followed an interval of duration  $4hr$  of strongly northward IMF when  $\Phi_D$  was essentially zero. This is slightly lower than the lowest reported  $F_{PC}$  that we know of in the literature ( $0.08GWb$ ), which may indicate our value for  $\tau_N$  is slightly too low. Nevertheless, the  $\tau_N$  used in Figure 7 does give a range of  $F_{PC}$  values that matches distribution previously reported in the literature. It is worth noting that panel (c) of Figure 7 shows that the solar wind dynamic pressure,  $p_{SW}$  is raised above previous levels at this time and, as mentioned above, this could have enhanced  $\Phi_{N2}$ , reducing  $F_{PC}$  values.

Figure 7e gives the modelled dawn-dusk polar cap diameter  $d_{PC}$  predicted using the assumption that the polar cap remains circular. We here used the dawn-dusk diameter deduced from DMSP/SSUSI images only as a rough check on that modelling. A major reason it can be of no greater significance than this is that, in reality, the polar cap is far from circular at some times. This is illustrated by Part (a) of Figure 8. This shows the aurora as seen by the F-17 satellite during a pass over the quiet, contracted polar cap in the northern hemisphere at  $07:18 UT$  on d-o-y 33: this is during the descent towards the deep minimum in  $F_{PC}$  at  $UT = 9.5hrs$  noted above. This pass reveals a horse-collar aurora with the putative OCB marked by narrow arcs that are almost parallel to the noon-midnight meridian (Wang et al., 2022). The polar cap is very far from circular at this time. Figure 8d shows a later pass at  $01:56UT$  on d-o-y 33, close to the time of the arrival of the first CME. The horse-collar form is still present and the dawn-dusk dimension of the dark polar cap gives a value of  $d_{PC}$  that is shown by the orange point in Figure 8e: this is lower than the value predicted for a circular polar cap because of

748 the horse-collar form is still present to some degree. In general, polar caps becomes more  
 749 circular as the open flux increases. The other panels of Figure 8 give examples. Parts  
 750 (c), (b) and (f) are northern hemisphere passes for, respectively, small, moderate and  
 751 large open flux, in which the observed part of the polar cap is more circular in form.  
 752 Part (e) is an example of a southern hemisphere pass of F-17 over a relatively large polar  
 753 cap. Southern hemisphere passes of both F-17 and F-18 tend to be toward the night-  
 754 side. We use passes where the poleward edge of the aurora is detectable within 1 hr of  
 755 the dawn-dusk MLT meridian and extrapolate the poleward boundary over up to 1 hr  
 756 of MLT if it does actually cross the meridian in the observed swathe. We apply  $\delta\Lambda$  of  
 757  $1^\circ$  at both 18 and 06 MLT. The results are shown for passes of F-17 and F-18 over the  
 758 northern and southern hemisphere polar caps by, respectively, red and blue points in Fig-  
 759 ure 8e. Cases where the polar cap is far from circular, such as in parts (a) and (d) are  
 760 not used. The results show considerable scatter which is readily explained by the changes  
 761 in shape of the polar cap, but do reveal the polar cap expansion and contraction dur-  
 762 ing and after the CME impacts. They also provide confirmation that the value for  $\tau_N$   
 763 used is appropriate.

764 The variations in the nightside voltage  $\Phi_N$  and the polar cap flux  $F_{PC}$  in Figure  
 765 7 follow that in the magnetopause voltage  $\Phi_D$  in ways that we would expect. Towards  
 766 the end of d-o-y 30 there is a sharp rise in  $\Phi_D$  that is followed by a similar, but smaller,  
 767 rise in  $\Phi_N$ . The high  $\Phi_D$  persists for almost a day, declining only slightly. The mismatches  
 768 in these voltages causes the polar cap flux  $F_{PC}$  to rise to a peak of  $0.68GWb$  at  $8.4 UT$   
 769 of d-o-y 31 and then fall back to its initial value near  $0.26GWb$ . This day-long event ap-  
 770 pears to be a period of driven convection and there is a slight rise in the *-SML*-related  
 771 nightside reconnection voltage  $\Phi_{N1}$  at its end. The next interesting feature is a sharp  
 772 spike in  $\Phi_D$  just before the end of d-o-y 32. This generates a response in *-SML* and hence  
 773  $\Phi_{N1}$  and the rise in  $F_{PC}$  is small and short-lived. This appears to be a small isolated  
 774 substorm cycle in which *-SML* does not rise above  $478nT$ . The decay in  $F_{PC}$  to the deep  
 775 minimum discussed above occurs after this event: we see  $\Phi_D$  and *SML* fall to essentially  
 776 zero for almost a day and the exponential decay of open flux due to  $\Phi_{N2}$  can clearly be  
 777 seen. After this, a second, stronger isolated substorm cycle occurs in which *-SML* rises  
 778 to  $763nT$  but, again, the rise in  $F_{PC}$  is small and short-lived.

779 It is after this that CME1 arrives.  $\Phi_D$  ramps up considerably, as does *-SML* and  
 780  $\Phi_{N1}$  but with a lag and by a smaller degree so the open flux grows to a peak of  $1.01GWb$ .  
 781 The *SML* index shows a series of spikes that suggest substorms, but  $\Phi_D$  is large and keeps  
 782 increasing, causing it to always exceed  $\Phi_N$  and so  $F_{PC}$  keeps rising. Only after the CME  
 783 has passed and  $\Phi_D$  declines sharply does  $\Phi_N$  dominate and reduce the open flux. This  
 784 rapid decline is caused by the loss rate  $\Phi_{N1}$  but between enhancements in *-SML* we see  
 785 that  $\Phi_{N2}$  also contributes. Again we note that in this interval between CME1 and CME2  
 786 Figure 7c shows considerably enhanced  $p_{SW}$  and this may have contributed to the de-  
 787 cline in  $F_{PC}$  by enhancing  $\Phi_{N2}$ .

788 CME 2 is somewhat different. The rises in  $\Phi_D$ ,  $\Phi_N$  and *-SML* are more modest than  
 789 in CME1. Again spikes in *SML* suggest a series of substorms. For this second event, the  
 790 response in  $\Phi_N$ , is slower and so  $F_{PC}$  grows to levels that slightly exceed those attained  
 791 in CME1 ( $1.04GWb$ ), even though the driving voltage  $\Phi_D$  is not as large in this second  
 792 event. Towards the end of the passage of CME2,  $\Phi_D$  and  $\Phi_N$  are approximately balanced  
 793 and the peak open flux is maintained. After the passage of CME2, intermittent  $\Phi_D$  means  
 794 that the decline in  $F_{PC}$  takes considerably longer and *-SML* remains low so the slow de-  
 795 cline in  $F_{PC}$  is associated with  $\Phi_{N2}$  more than  $\Phi_{N1}$ .

796 It is useful to look at the relative contributions of the two open flux loss rates  $\Phi_{N1}$   
 797 and  $\Phi_{N2}$ . Figure 9 looks at the relationship of the two. Comparison of Parts (a) and (d)  
 798 of Figure 9 shows that, in general,  $\Phi_{N1}$  is greater than  $\Phi_{N2}$ . Both increase with increas-  
 799 ing transpolar voltage  $\Phi_{PC}$  and hence the sum of the two does the same (Figure 9b). Part  
 800 (e) shows the ratio of the two,  $\Phi_{N1}/\Phi_{N2}$ , as a function of  $\Phi_{PC}$ , the mauve line is unity

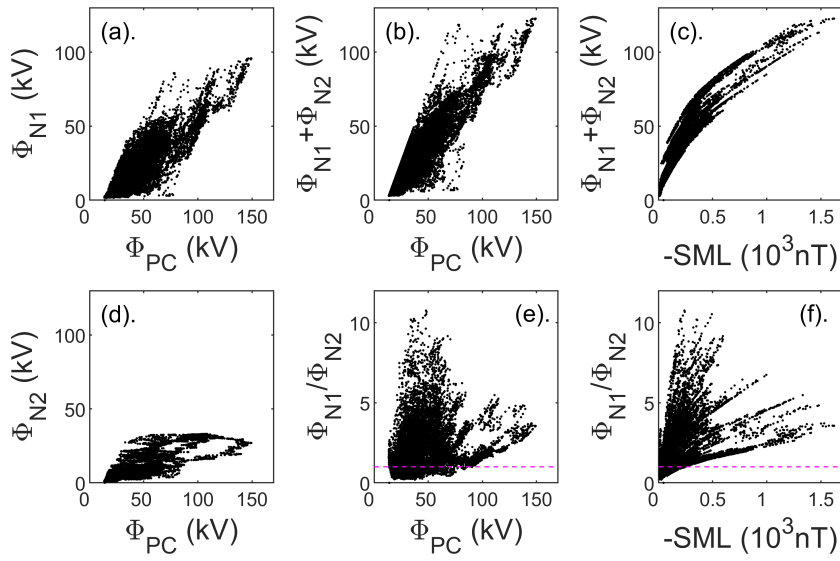


**Figure 9.** Scatter plots comparing the open flux loss rates associated with the nightside auroral electrojet,  $\Phi_{N1}$ , and that associated with enhanced tail magnetic flux but without a signature in enhanced auroral electrojet activity,  $\Phi_{N2}$ . Parts (a), (d), (b) and (e) show, as a function of transpolar voltage  $\Phi_{PC}$ : (a)  $\Phi_{N1}$ ; (d)  $\Phi_{N2}$ ; (b) the total loss rate,  $\Phi_N = \Phi_{N1} + \Phi_{N2}$ , and (e) the ratio of the two,  $\Phi_{N1}/\Phi_{N2}$ . (c) and (f) show, respectively, the sum and the ratio of the two loss voltages as a function of the  $-SML$  value. Data are for the “calibration interval” between the two vertical dashed lines in Figure 7. Mauve dashed lines in parts (e) and (f) show where the two loss rates are equal.

801 for this ratio and so  $\Phi_{N1}$  always dominates for  $\Phi_{PC} \geq 85kV$ . Figure 9f is the same ra-  
 802 tio as a function of  $-SML$  and shows that  $\Phi_{N1}$  always dominates for  $-SML \geq 27nT$ ; how-  
 803 ever, the plot also shows great variability in this ratio which is the effect of the amount  
 804 of open flux  $F_{PC}$  on  $\Phi_{N2}$ . This is also seen in Figure 9c which plots the total loss rate  
 805 as a function of  $-SML$ . This reveals the form of  $\Phi_{N1}$  given by Equation 6, but that  $\Phi_{N2}$   
 806 has indeed added scatter; however, the scatter in Figure 9c is not as great as in Figure  
 807 3 because it is for 7 days of 1-minute data whereas Figure 3 is for 25 years of hourly data.

808 We conclude that the loss rate of open flux is largely dependent on the  $SML$  au-  
 809 roral electrojet index and although the loss  $\Phi_{N2}$  that is not captured by  $SML$  is relatively  
 810 small, it is still important for the application of the ECPC model because otherwise es-  
 811 timated open fluxes rise to levels that are not seen in the real magnetosphere.

812 It is interesting to note that Figure 7d shows that the open flux  $F_{PC}$  between the  
 813 CMEs fell to  $0.20GWb$ , just below the value at the start and end of the calibration in-  
 814 terval. This eliminates preconditioning effects of CME1 on the response to CME2, at least  
 815 in terms of residual open flux. In this context, we also note that Figure 5c shows that  
 816 the ring current indices  $-SMR$  and  $-SYM-H$  fell back down after CME1 to only just above  
 817 their values before the arrival of CME1. (Their decay after CME2 was noticeably slower).  
 818 This argues against major preconditioning in terms of ring current energy as well. There  
 819 are other possible pre-conditioning effects such as the thickness of the plasma sheet and  
 820 the speeds of polar thermospheric winds. The latter, however, would tend to reduce the  
 821 heating effect of CME2 not increase it.

## 822 5 The Effect of Earth's eccentric magnetic field

823 The previous section shows that the polar cap expanded and contracted during the  
 824 events in early February 2022. In this section we add to the effects of this the  $UT$  vari-  
 825 ations caused by the diurnal rotation of Earth's eccentric magnetic field. The motions  
 826 are computed using the eccentric dipole model of the geomagnetic field by Koochak and  
 827 FraserSmith (2017), as discussed by Lockwood et al. (2021).

828 Figure 10 demonstrates the effect of polar cap motions. Panel (a) shows the trans-  
 829 polar voltage  $\Phi_{PC}$  computed using Equation 2 from the variations of  $\Phi_D$  and  $\Phi_N$  (with  
 830 constant  $\Phi_V$ ) derived in the previous section. Part (b) shows the dawn-dusk voltages in-  
 831 duced in the north and south polar cap, in a geocentric frame, by the diurnal cycle of sun-  
 832 ward/antisunward polar cap motion, respectively  $\phi_{MN}$  and  $\phi_{MS}$ . Note that for constant  
 833 dawn-dusk polar cap diameter, these would be sine waves and the dashed lines give the  
 834 variation for the mean of the polar cap diameter over the calibration interval  $\tau$ ,  $\langle d_{PC} \rangle_\tau =$   
 835  $3.08Mm$  (roughly equivalent to a latitudinal polar cap angular radius of  $13^\circ$ ). Note also  
 836 that the amplitude of the sine wave is smaller for the northern hemisphere because the  
 837 offset of the rotational and magnetic pole is smaller in the north and that the sine waves  
 838 are not in antiphase because for the eccentric dipole field model used the magnetic poles  
 839 are not  $180^\circ$  apart in longitude (as they would be for a geocentric dipole).

840 Figure 10c shows the average transpolar voltage allowing for the motions of both  
 841 polar caps, computed using Equations 10 and 11 for the northern and southern hemi-  
 842 sphere,  $\Phi'_{NC}$  and  $\Phi'_{SC}$  shown in red and blue, respectively. The black line is the aver-  
 843 age of the two,  $\Phi'_{PC}$  which is different from the transpolar voltage in the absence pole  
 844 motions  $\Phi_{PC}$ , which is shown in Figure 10a and by the grey area in Figure 10c. If  $\Phi'$   
 845 in a hemisphere is smaller than  $\Phi_{PC}$  it means that polar cap is moving towards the Sun.  
 846 Let us apply Faraday's law to a loop PCGS, fixed in a geocentric-solar frame, where P  
 847 and C are the dawn and dusk flanks of the ionospheric polar cap which map along open  
 848 geomagnetic field lines to the points G and S, respectively, just outside the bow shock  
 849 in interplanetary space, often referred to as the "Stern Gap", SG (see Lockwood & Cow-  
 850 ley, 2022). The antisunward flow of the solar wind, with frozen-in open magnetic field,

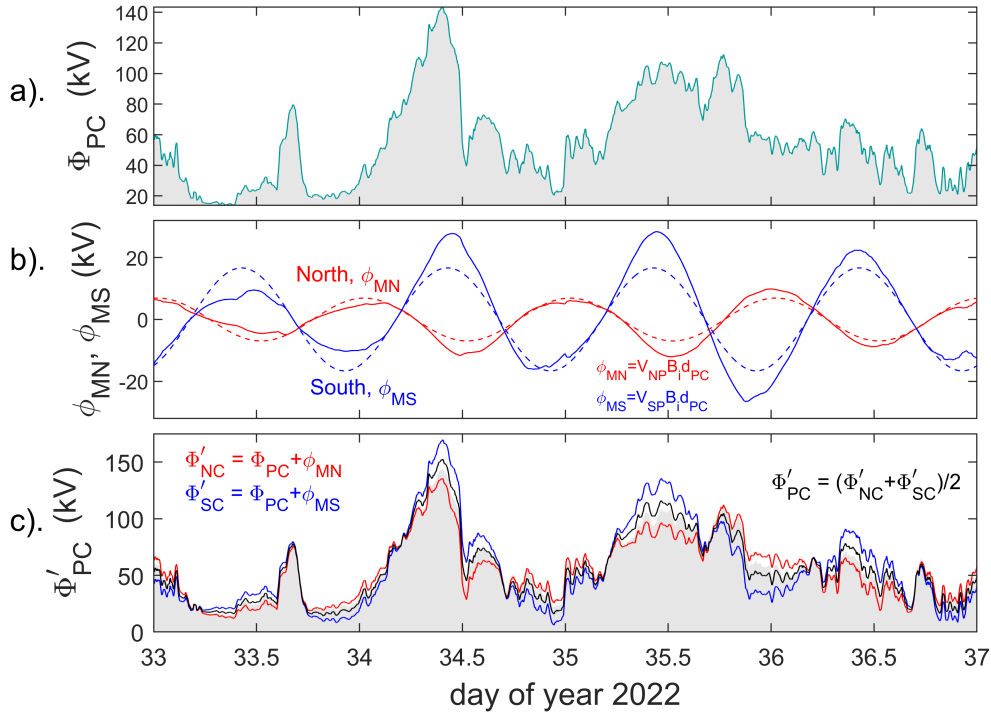


**Figure 10.** Analysis of the effect of pole motions on transpolar voltage during the events of early February, 2022. (a). The transpolar voltage derived from Equation 2,  $\Phi_{PC}$ . (b). The voltages across the northern ( $\phi_N$ , in red) and southern ( $\phi_S$ , in blue) polar caps in a geocentric-solar reference frame (such as GSM or GSE) induced by the diurnal motions of the poles (see Equations 10 and 11). Note that these variations would be sinusoidal if the polar cap diameter  $d_{PC}$  were constant (see Lockwood et al., 2021) but here depart from sine waves because we apply the modelled variations in  $d_{PC}$  shown in Figure 7d. The dashed lines are the variations for the mean value of the polar cap diameter over the calibration interval  $\tau$ ,  $\langle d_{PC} \rangle_\tau = 3.08Mm$ . (c). The variations in voltages in the GSE/GSM frames allowing for pole motions in the northern hemisphere,  $\Phi'_{NC}$  (in red) and in the southern hemisphere,  $\Phi'_{SC}$  (in blue). The black line is the average of the two ( $\Phi'_{PC}$ ) and the grey area gives the uncorrected voltage,  $\Phi_{PC}$ , repeated from panel (a) to aid comparison.

851 between S and G adds to the magnetic flux threading the loop PCGS and the sunward  
 852 convection of frozen-in field in the F-region ionosphere between P and C removes flux  
 853 from that loop. Hence if sunward polar cap bulk motion is slowing the rate that mag-  
 854 netic flux is transferred antisunward across PC in the ionosphere, it is reducing the rate  
 855 at which flux removed from the loop. Hence this situation means that less energy is being  
 856 directly deposited in the ionosphere but more magnetic energy is being stored in that  
 857 hemisphere of the tail lobe. Conversely, If  $\Phi'$  exceeds  $\Phi_{PC}$ , the polar cap is moving away  
 858 from the Sun (i.e. with the solar wind) so that more energy is being directly deposited  
 859 in ionosphere but less energy is being stored in that hemisphere of the tail lobe.

860 It is worth noting that some of these diurnal cycles may have been missed in some  
 861 magnetometer observations of geomagnetic activity as they were attributed to the Sq  
 862 variation. This is because to reveal geomagnetic activity, magnetometer data usually has  
 863 subtracted from it a quiet diurnal variation to remove the effects of dynamo action, of  
 864 particular, solar thermal tides and the equatorial electrojet that give the Sq variation  
 865 (Yamazaki & Maute, 2017). The polar cap diameter  $d_{PC}$  will be small in quiet times but  
 866 not zero and so the pole motions effect may have added to the quiet day diurnal vari-  
 867 ation that is subtracted. This is most likely to be the case inside the polar cap and so  
 868 a factor for the Polar Cap Indices (*PCI*). We searched for an effect of the different pol-  
 869 ar motions during this event in the published provisional Northern and Southern hemi-  
 870 sphere *PCI*. Their variations are both very similar to the *-SML* index and so appear to  
 871 be dominated by the auroral electrojet in this event. We note that some other studies  
 872 have almost certainly detected signatures of the pole-motion effect but have generally  
 873 attributed it to ionospheric conductivity effects.

## 874 6 The Importance of the Universal Time of CME arrival

875 Owens et al. (2020) have discussed the value of accurate prediction of the arrival  
 876 time of CME impacts on Earth's magnetosphere. They make the point that if false-alarms  
 877 are a serious problem, accurate arrival time information is only valuable if the geoeffec-  
 878 tiveness of the CME can also be forecast. The analysis presented in this paper adds a  
 879 further complication to that discussion in that the geoeffectiveness of a CME is shown  
 880 to depend upon the Universal Time of the CME arrival.

881 To investigate the effect of pole motions in isolation, we here consider that the volt-  
 882 ages  $\Phi_D$  and  $\Phi_N$  would not depend on the Universal Time of the CME impact. The phase  
 883 of the diurnal cycles of pole motions have an influence on geoeffectiveness through the  
 884 modification of  $\Phi_{PC}$  to  $\Phi'_{NC}$ ,  $\Phi'_{SC}$  and  $\Phi'_{PC}$ .

885 However, in reality, the dipole tilt (and hence Universal Time) will influence  $\Phi_D$   
 886 through its effect on the magnetic shear at, and length of, the magnetopause reconec-  
 887 tion X-line via the Russell-McPherron (R-M) effect (Russell & McPherron, 1973; Lock-  
 888 wood, Owens, Barnard, Haines, et al., 2020). In our synthesis of the effects of a delayed  
 889 arrival of a CME, we allow for this by lagging (by a delay  $\delta t$ ) the variations in the fac-  
 890 tors  $B_{\perp}$ ,  $\rho_{sw}$ , and  $V_{sw}$  in Equation 5; however, the term  $\sin^d(\theta/2)$  cannot be simply lagged  
 891 in the same way. The reason is that the clock angle  $\theta$  is computed in the GSM frame and  
 892 because of the *UT* variation in the rotation angle  $\gamma$  between the GSE and GSM frames  
 893 (caused by the dipole tilt variation with *UT*), the lagged values of IMF in the GSE frame,  
 894  $[B_Z]_{GSE}$  and  $[B_Y]_{GSE}$ , have to be transformed for the  $\gamma$  of the new *UT* into  $[B_Z]_{GSM}$   
 895 and  $[B_Y]_{GSM}$  that are then used to compute  $\theta = \tan^{-1}(|[B_Y]_{GSM}|/[B_Z]_{GSM})$  and hence  
 896  $\sin^d(\theta/2)$  and  $\Phi_D$  for the delayed arrival at Earth.

897 In general, there will probably also be *UT* effects on  $\Phi_N$ . A number of papers have  
 898 discussed mechanisms by which the dipole tilt can influence tail structure and dynam-  
 899 ics and so introduce *UT* effects into reconnection responses in the tail (Kivelson & Hughes,  
 900 1990; Danilov et al., 2013; Kubyshkina et al., 2015; Lockwood, Owens, Barnard, Watt,

et al., 2020; Lockwood et al., 2021). However as these effects are less well established than the R-M effect, we here simplify by investigating the effect of dipole tilts on  $\Phi_D$  only. We do this by assuming the form of the temporal variation in  $\Phi_N$  response is the same as for the unlagged  $\delta t = 0$  case, as shown in Figure 7. This allows us to simply lag the  $\Phi_N$  variation by  $\delta t$ . We then scale these lagged values of  $\Phi_N$  so that the integral over the calibration interval (which is also lagged by  $\delta t$ ) is equal to that of the recalculated, lagged  $\Phi_D$ . This gives us the revised variation of  $\Phi_{PC}$  for the  $\delta t$  considered, from Equation 2. We can study the R-M effect in isolation from this  $\Phi_{PC}$  variation but also transform it into  $\Phi'_{PC}$  (by evaluating  $\Phi'_{NC}$  and  $\Phi'_{SC}$  and averaging them) to study the combined effect of the R-M effect and the pole motions.

Figure 11a shows four variations associated with the CME events. These are: (1) the observed *SYM-H* geomagnetic index (in mauve); (2) the power deposited globally in the ionosphere and thermosphere by Joule heating,  $P_i$ , as modelled by Dang et al. (2022) (in green); (3) the square of the voltage derived here from the ECPC model but not allowing for polar cap motions  $\Phi_{PC}^2$  (in orange); and (4) the square of the transpolar voltage derived here when polar cap motions are included  $[\Phi'_{PC}]^2$  (in black). All four variations have been normalised to the large peak that occurred towards the end of CME1 and all are for no introduced synthetic lag (i.e.,  $\delta t = 0$ ). The power input predicted by Dang et al.,  $P_i$ , has been lagged by  $0.6hrs$  in this plot to give optimum agreement, we presume this accounts for propagation and response lags. We can see that, with this lag,  $P_i$  agrees very well with the variations in  $\Phi_{PC}^2$  and  $[\Phi'_{PC}]^2$  predicted here.  $P_i$  was derived from the observed solar wind and IMF parameters using the statistical and empirical convection model of Weimer (2005). If we use a simple resistor analogy the power deposited is proportional to the square of the voltage and so the square of the transpolar voltage is a simple proxy metric of Joule heating rate and indeed Robinson and Zanetti (2021) do find a good statistical square-law relationship between the two for the 27 geomagnetic storm events that they studied (see their Figure 2d). Hence the use of a steady-state convection model, driven by the upstream solar wind and IMF, yields a very similar global heating variation to that inferred here using the ECPC model. Note that *SYM-H* is of relevance to magnetospheric energetics being related to the energy content of the ring current; however, that relationship is not a straightforward one (Sandhu et al., 2021; Robinson & Zanetti, 2021). Of interest in the time series studied here is the fact that peaks in Joule heating of the ionosphere after each CME are associated with the time of enhanced auroral activity as identified by the bursts of enhanced *-SML* and enhanced  $\Phi_N$ . However, a lower level of Joule heating does continue after *-SML* declines when *SYM-H* remains enhanced and the polar cap flux  $F_{PC}$  is decaying slowly. This appears to be due to the “quiet” open flux loss that is not associated with *SML* and energy stored in the tail lobes is quietly (without auroral electrojet activity) deposited in both the ionosphere and ring current.

Figure 11a shows that the proxy for global heating rate from our analysis  $[\Phi'_{PC}]^2$  is similar to the results of Dang et al. (2022) who employed the steady-state empirical model of transpolar voltage and Joule heating by Weimer (2005). However, Figure 11b shows there is a major difference. The Weimer model predicts the same transpolar voltage in the two polar caps and only some dipole tilt effects on conductivity would give any difference in Joule heating between the two hemispheres. We here predict that both the transpolar voltage and the Joule heating have strong Universal Time variations that are close to being in antiphase in the two polar caps. The precise behaviour depends on the Universal Time of the storm-time rise in  $\Phi_D$  and that is one reason why CME1 and CME2 have such different effects in these events. Figure 11b shows that during CME1 the two hemispheres show similar temporal variations in  $[\Phi'_{NC}]^2$  and  $[\Phi'_{SC}]^2$  but the southern hemisphere value is considerably larger. During CME2,  $[\Phi'_{SC}]^2$  again dominates initially but for the peak at the end of the passage of CME2 the Joule heating is dominated by  $[\Phi'_{NC}]^2$ . Therefore, although the two methods predict very similar global Joule heating power, the temporal variation of the deposition into the two polar caps is more com-

plex in our analysis. The behaviour during CME2 is more complex than for CME1 because, in addition to the pole motions, the  $\Phi_N$  rise is delayed after the causal rise in  $\Phi_D$  (see Figure 7a).

The bottom panel of Figure 11 shows the combined effect of introducing synthetic lags  $\delta t$  in arrival time at Earth in the range [0:2:12] hrs, via both the R-M and pole-motion effects. It shows the  $[\Phi'_{PC}]^2$  variations for each value of  $\delta t$ , derived as described above.

Figure 11c demonstrates that the peak  $[\Phi'_{PC}]^2$  at the end of CME1 would have been considerably smaller if the event had arrived some hours later. Figure 12 analyses the relative contribution of the R-M effects and the pole motions to the combined variation with arrival time shifts  $\delta t$  between -12 hrs and +12 hrs ( $\delta t = [-12:0.1:12]$ hrs). The event is here taken to be between the start of d-o-y 34 and d-o-y 36.5 (in unshifted time) which runs from the start of CME1, to near the end of the recovery from CME2. Figure 11a shows that  $[\Phi'_{PC}]^2$  is a plausible approximate proxy for the global Joule heating rate and the maximum and event-integrated values are computed for each value of  $\delta t$ . Part (a) of Figure 12 shows the variations for the peak  $[\Phi'_{PC}]^2$  which occurs at the end of CME1. Part (b) shows the integral of  $[\Phi'_{PC}]^2$  over the event interval, as defined above. It can be seen in Part (a) that the R-M effect (in mauve) is relatively minor for the induced  $UT$  changes in the peak power deposited, the total variation (in black) of the peak being dominated the pole-motion effect (in green). In this case, the R-M effect causes the opposite effect on the peak to the pole motion: this is not a general result, for example, the R-M effect would be reversed if the IMF  $[B_Y]_{GSE}$  had the opposite polarity. Hence the two effects tend to cancel in this case, but because the pole-motion effect is larger the net effect is still considerable. However for the integrated power deposited by the two CMEs, shown in Part (b), the variations caused by the two effects are more similar in amplitude and not so close to being in antiphase and the net effect is smaller but still present.

The combination of the two effects causes a variation in the peak  $[\Phi'_{PC}]^2$  between 82.7% at  $\delta t = 10.8hrs$  (and at  $\delta t = -13.2hrs$ ) and 100.4% at  $\delta t = 0.8hrs$  showing that the CME events arrived at almost the optimum  $UT$  for generating maximum heating effect in the thermosphere and that the peak would have been 17.3% smaller if the the event had arrived 13.2 hours earlier or 10.8 hours later. It should be noted that the R-M effect depends on the temporal variation of the IMF Y and Z components in GSE just before or after the peak (for  $\delta t > 0$  and  $\delta t < 0$ , respectively, and so the R-M effect on the peak in other events could be considerably different. The integrated power over the event varies between 92.5% at  $\delta t = -11.6hrs$  (and 12.4 hrs) and 100.05% at  $\delta t = 0.2hrs$ . This is a smaller effect than that on the peak value but still considerable.

It is interesting that the maximum in both curves is close to  $\delta t = 0$ , which shows that the thermospheric heating would have been smaller had the CMEs arrived at almost any other  $UT$ . To understand the full implications for the space weather event would require numerical modelling of the coupled ionosphere-thermosphere system for the various  $UT$  of event arrival with allowance for the  $UT$ -dependent total power deposition, and for the  $UT$ -dependent division of that power between the two hemispheres. Without such modelling it is not possible to say how critical to the outcome the  $UT$  of event arrival was. Nevertheless, it is interesting to note that 11 of the 40 satellites launched did reach their intended orbit, almost certainly because by the time of the event they were the ones had been sufficiently elevated in altitude (Tsurutani et al., 2022). This strongly implies that fewer of the satellites would have been lost had the event occurred at a different  $UT$ .

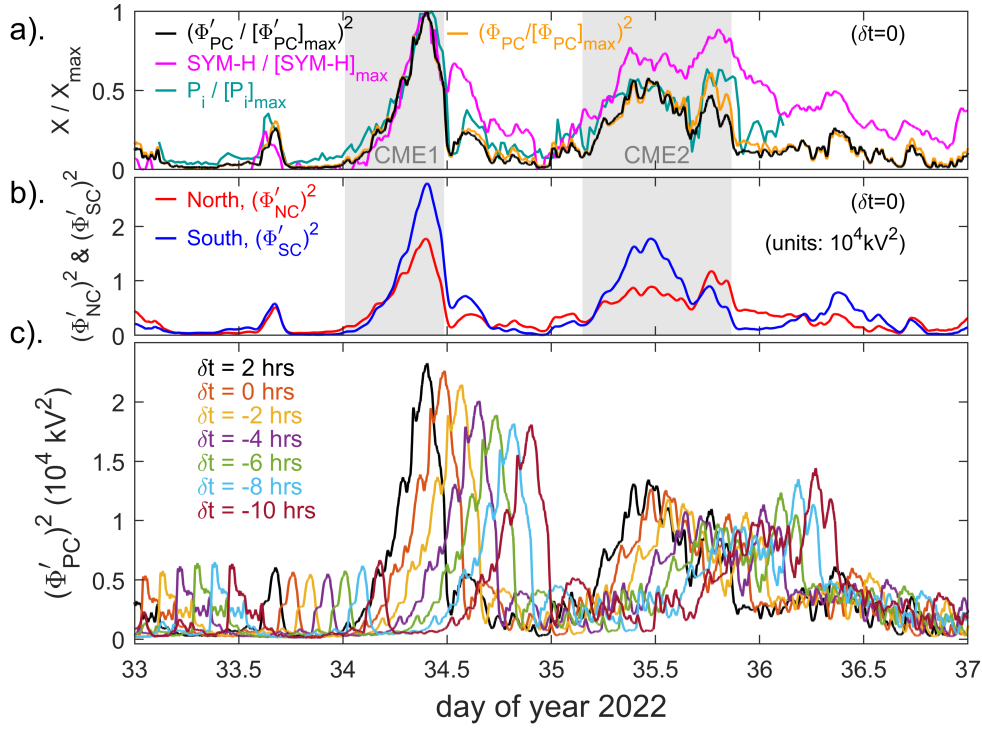


**Figure 11.** Analysis of the effects of CME arrival time. (a) shows (in mauve) the variation of the *SYM-H* geomagnetic index; (in green) the power deposited in the auroral ionospheres,  $P_i$ , as modelled for these events by (Dang et al., 2022) using the empirical transpolar voltage and Joule heating model of (Weimer, 2005); (in orange) the square of the transpolar voltage neglecting pole motions, as shown in green in Figure 10a,  $\Phi_{PC}^2$ ; and (in black) the square of the average polar voltage with pole motions, as shown in black in Figure 10c,  $[\Phi'_{PC}]^2$ . All four are normalised by their peak value towards the end of the passage of CME1 and all three are shown in the panel without any synthetic lag  $\delta t$  being introduced other than for  $P_i$  which has been lagged by 0.6hrs. (b). shows the variations of the square of the transpolar voltages in the northern and southern polar caps allowing for pole motions,  $[\Phi'_{NC}]^2$  and  $[\Phi'_{SC}]^2$ , respectively. In (c) the interplanetary data sequences are lagged by  $\delta t$  but the IMF orientation factor in GSM recomputed for the different *UT* of arrival in evaluating  $\Phi_D$  (the Russell-McPherron effect, R-M) as well as the different phase of the diurnal cycles of pole motions (the pole motion effect). The response of the nightside reconnection voltage  $\Phi_N$  is assumed to be the same in waveform (but lagged by  $\delta t$ ) as that for  $\delta t = 0$  but is scaled such that the integral over the calibration interval matches the integrated revised  $\Phi_D$ . For each lag  $(\Phi'_{NC})$  and  $(\Phi'_{SC})$  are computed. The plot shows the square of the average of the two,  $[\Phi'_{PC}]^2$  as a function of time for  $\delta t$  which is varied between 0 (black line, as also shown in part a) and 12hrs (blue line).

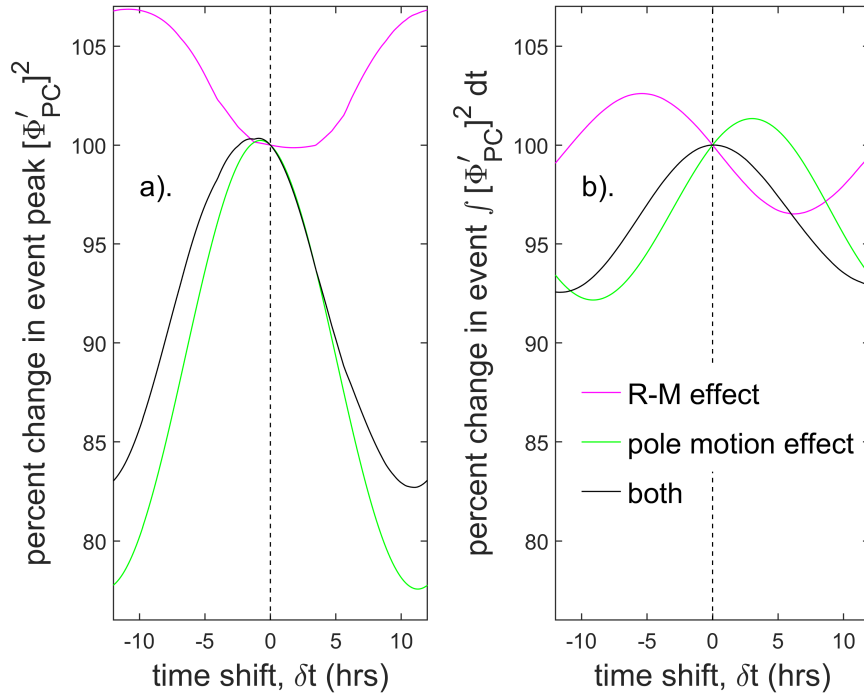


**Figure 12.** The computed effect of variation in the  $UT$  of arrival of the interplanetary disturbance on the  $[\Phi'_{PC}]^2$  proxy for thermospheric Joule heating rate. The mauve lines show the effect of  $\delta t$  on  $[\Phi'_{PC}]^2$  via the R-M effect and the green lines show the effect via the phase of the diurnal pole motions. The black lines show the combination of both effects. All three are shown as a function of the synthesised lag in the  $UT$  of the events' arrival,  $\delta t$ . (a) shows the variations in the amplitude of the large peak in  $[\Phi'_{PC}]^2$  at the end of CME1 and (b) shows the variations for the integral of  $[\Phi'_{PC}]^2$  over the lagged event (between decimal day of year  $34 + \delta t/24$  and  $36.5 + \delta t/24$ , where  $\delta t$  is in hours).

## 7 Discussion and Conclusions

The introduction to this paper gave the occurrence probability of events of the magnitude of the 3-4 February 2022 events in the *kp* and *am* geomagnetic index datasets that extend back to 1932 and 1959, respectively. These probabilities were 3.5% for *kp* and 2% for *am*. We have near-continuous IMF (with continuous *SML* data) since 1995 and to compare with the geomagnetic data occurrence statistics it is important to use the subset of the index datasets over the same interval. The reason is that the decline in the open solar flux since 1985 has caused a similar long-term decline in geomagnetic activity (Lockwood et al., 2022). The *kp* and *am* indices after both the CME impacts in the events studied here peaked at 5+ and 84nT, levels that have been detected or exceeded, for, respectively, 1.22% and 1.13% of the years 1995-2021, inclusive. The figure for the *am* index is the most significant because it has the most uniform response to solar wind forcing with time-of-year and Universal Time of all the geomagnetic indices because it employs the most uniform geographical network of stations, using two hemispheric rings of near-equispaced mid-latitude stations (Lockwood, Chambodut, et al., 2019).

It is interesting to compare with the *-SML* index which, in 10-minute running means, peaked at 1348nT and 1059nT after CME1 and CME2, respectively. These values have been detected or exceeded 0.06% and 0.21% of the interval 1995-2021. Notice that the choice of 10 minutes is somewhat arbitrary and the corresponding values for the raw 1-minute *-SML* data are 0.03% and 0.09%; however, the maximum *-SML* in 1-minute data is not a good measure of the integrated thermospheric heating effect in the event. For 1-hour running means the values are 0.06% and 0.23% which are very similar to the 10-min values. Similarly the 10-minute running means of the inferred dayside magnetopause reconnection voltage  $\Phi_D$  peaked at 148.2kV and 103.7kV after CME1 and CME2, values that were found for 0.13% and 0.63% of the same interval. Hence the events were significantly more unusual and extreme in the 1-minute *-SML* and  $\Phi_D$  values than in the 3-hourly planetary indices.

We have here investigated the magnetospheric response to the two CMEs that impacted Earth on 3 and 4 February 2022 and famously led to the loss of many recently-launched Starlink satellites. Using statistical relationships to derive the variations in reconnection rate in the dayside magnetopause and in the cross-tail current sheet from the observed variations of interplanetary space and of the *SML* auroral electrojet index. We find that, in addition to a loss rate of magnetospheric open flux related to *SML*, that a smaller loss rate, not detected by *SML* but proportional to the open flux is needed to prevent unfeasibly large polar cap fluxes (above about 1 GWb). Using a loss rate time constant of  $\tau_N = 6.8\text{min}$  we match the polar cap diameters inferred from auroral images, making the simplifying assumption of a circular polar cap.

The dawn-dusk diameter of the open polar cap inferred in this way was then used to compute the voltage contributions made by the diurnal pattern of polar cap motions in a geocentric-solar frame. This voltage was then combined with that due to the solar wind-magnetosphere interaction, which also depends on *UT* because of the well-understood Russell-McPherron effect. This has enabled us to compute what the transpolar voltage and Joule heating responses would have been, had the CMEs arrived at different Universal Times.

We have shown that the CMEs in the events of early February 2022 arrived at close to the Universal Time which gave optimum heating of the thermosphere. This is particularly true for the peak of the heating burst at the end of the first CME, but is also true for the integrated heating over the duration of both CME events and their immediate aftermath. We show that the heating peak could have been lower by up to 17.3%, and the integrated heating lower by up to 7.5%, had the events arrived roughly 12 hours earlier or 12 hours later. It is not possible from the study presented here to make definitive statements about what difference this would have made to the fate of the Starlink

1055 satellites. However, our results could be used with numerical modelling of the coupled  
1056 ionosphere-thermosphere system to evaluate how the  $UT$  of event arrival could have in-  
1057 fluenced the subsequent orbit changes. This modelling would need to take account of the  
1058  $UT$ -dependent total power deposition, and for the  $UT$ -dependent division of that power  
1059 between the two hemispheres. Hence, at this stage, it is not possible to say how criti-  
1060 cal to the outcome for the satellites the  $UT$  of event arrival was. Nevertheless, noting  
1061 that 11 of the 40 satellites launched did reach their intended orbit does strongly suggest  
1062 that more would have survived had the events occurred at a different  $UT$ . We note that  
1063 the modelling of the heating during this event by (Dang et al., 2022) shows that there  
1064 is structure in MLT, latitude (including the hemisphere). The phenomena we describe  
1065 has implications for this structure which will only be resolved by further modelling, al-  
1066 lowing for the  $UT$  dependence of the Joule heating and the differences between the two  
1067 hemispheres.

1068 This adds another dimension to the prediction and understanding of terrestrial space  
1069 weather events: we have known for many years that we need to develop techniques to  
1070 better predict the IMF field strength and orientation embedded in events, but we need  
1071 to also predict the time-of arrival with some accuracy to make best use of that informa-  
1072 tion and predict the geoeffectiveness of the event.

1073

## References

1074

1075

1076

1077

1078

1079

1080

1081

1082

1083

1084

1085

1086

1087

1088

1089

1090

1091

1092

1093

1094

1095

1096

1097

1098

1099

1100

1101

1102

1103

1104

1105

1106

1107

1108

1109

1110

1111

1112

1113

1114

1115

1116

1117

1118

1119

1120

1121

1122

1123

1124

1125

1126

1127

- Anderson, B. J., Korth, H., Waters, C. L., Green, D. L., Merkin, V. G., Barnes, R. J., & Dyrud, L. P. (2014). Development of large-scale Birkeland currents determined from the Active Magnetosphere and Planetary Electrodynamics Response Experiment. *Geophysical Research Letters*, *41*(9), 3017–3025. Retrieved 2022-11-12, from <http://doi.wiley.com/10.1002/2014GL059941> doi: 10.1002/2014GL059941
- Atkinson, G. (1967). An approximate flow equation for geomagnetic flux tubes and its application to polar substorms. *Journal of Geophysical Research*, *72*(21), 5373–5382. Retrieved 2022-11-11, from <http://doi.wiley.com/10.1029/JZ072i021p05373> doi: 10.1029/JZ072i021p05373
- Atkinson, G. (1978). Energy flow and closure of current systems in the magnetosphere. *Journal of Geophysical Research*, *83*(A3), 1089–1103. Retrieved 2022-11-10, from <http://doi.wiley.com/10.1029/JA083iA03p01089> doi: 10.1029/JA083iA03p01089
- Baker, D. N., Pulkkinen, T. I., Hesse, M., & McPherron, R. L. (1997). A quantitative assessment of energy storage and release in the Earth's magnetotail. *Journal of Geophysical Research: Space Physics*, *102*(A4), 7159–7168. Retrieved 2022-11-12, from <http://doi.wiley.com/10.1029/96JA03961> doi: 10.1029/96JA03961
- Bartels, J. (1936). The eccentric dipole approximating the Earth's magnetic field. *Journal of Geophysical Research*, *41*(3), 225–250. Retrieved 2023-01-20, from <http://doi.wiley.com/10.1029/TE041i003p00225> doi: 10.1029/TE041i003p00225
- Bartels, J. (1949). The standardized index Ks and the planetary index Kp. *IATME Bulletin*, *12b*, 97.
- Bartels, J., Heck, N., & Johnston, H. (1939). The three-hour-range index measuring geomagnetic activity. *J. Geophys. Res.*, *44*, 411–454. Retrieved from <https://doi.org/10.1029/TE044i004p00411> doi: 10.1029/TE044i004p00411
- Billett, D. D., Grocott, A., Wild, J. A., Walach, M.-T., & Kosch, M. J. (2018). Diurnal variations in global Joule heating morphology and magnitude due to neutral winds. *Journal of Geophysical Research: Space Physics*. Retrieved 2022-11-10, from <http://doi.wiley.com/10.1002/2017JA025141> doi: 10.1002/2017JA025141
- Blockx, C., Grard, J.-C., Coumans, V., Hubert, B., & Meurant, M. (2009). Contributions of the driven process and the loading-unloading process during substorms: A study based on the IMAGE-SI12 imager. *Journal of Geophysical Research: Space Physics*, *114*(A2), n/a–n/a. Retrieved 2022-11-11, from <http://doi.wiley.com/10.1029/2008JA013280> doi: 10.1029/2008JA013280
- Boakes, P. D., Milan, S. E., Abel, G. A., Freeman, M. P., Chisham, G., & Hubert, B. (2009). A statistical study of the open magnetic flux content of the magnetosphere at the time of substorm onset. *Geophysical Research Letters*, *36*(4), L04105. Retrieved 2022-10-23, from <http://doi.wiley.com/10.1029/2008GL037059> doi: 10.1029/2008GL037059
- Boakes, P. D., Milan, S. E., Abel, G. A., Freeman, M. P., Chisham, G., Hubert, B., & Sotirelis, T. (2008). On the use of IMAGE FUV for estimating the latitude of the open/closed magnetic field line boundary in the ionosphere. *Annales Geophysicae*, *26*(9), 2759–2769. Retrieved 2022-11-01, from <https://angeo.copernicus.org/articles/26/2759/2008/> doi: 10.5194/angeo-26-2759-2008
- Borovsky, J. E., Lavraud, B., & Kuznetsova, M. M. (2009). Polar cap potential saturation, dayside reconnection, and changes to the magnetosphere. *Journal of Geophysical Research: Space Physics*, *114*(A3), n/a–n/a. Retrieved 2022-11-10, from <http://doi.wiley.com/10.1029/2009JA014058> doi: 10.1029/2009JA014058

- 1128 10.1029/2009JA014058  
 1129 Boudouridis, A. (2005). Enhanced solar wind geoeffectiveness after a sudden increase  
 1130 in dynamic pressure during southward IMF orientation. *Journal of Geophysical*  
 1131 *Research*, *110*(A5), A05214. Retrieved 2022-11-11, from [http://doi.wiley](http://doi.wiley.com/10.1029/2004JA010704)  
 1132 [.com/10.1029/2004JA010704](http://doi.wiley.com/10.1029/2004JA010704) doi: 10.1029/2004JA010704  
 1133 Bower, G. E., Milan, S. E., Paxton, L. J., & Anderson, B. J. (2022). Oc-  
 1134 currence statistics of horse collar aurora. *Journal of Geophysical Re-*  
 1135 *search: Space Physics*, *127*(5), e2022JA030385. Retrieved from [https://](https://agupubs.onlinelibrary.wiley.com/doi/abs/10.1029/2022JA030385)  
 1136 [agupubs.onlinelibrary.wiley.com/doi/abs/10.1029/2022JA030385](https://agupubs.onlinelibrary.wiley.com/doi/abs/10.1029/2022JA030385) doi:  
 1137 10.1029/2022JA030385  
 1138 Brambles, O. J., Lotko, W., Zhang, B., Oulette, J., Lyon, J., & Wiltberger, M.  
 1139 (2013). The effects of ionospheric outflow on ICME and SIR driven sawtooth  
 1140 events. *Journal of Geophysical Research: Space Physics*, *118*(10), 6026–6041.  
 1141 Retrieved 2022-10-28, from <http://doi.wiley.com/10.1002/jgra.50522>  
 1142 doi: 10.1002/jgra.50522  
 1143 Caan, M. N., McPherron, R. L., & Russell, C. T. (1973). Solar wind and substorm-  
 1144 related changes in the lobes of the geomagnetic tail. *Journal of Geophys-*  
 1145 *ical Research*, *78*(34), 8087–8096. Retrieved 2022-11-11, from [http://](http://doi.wiley.com/10.1029/JA078i034p08087)  
 1146 [doi.wiley.com/10.1029/JA078i034p08087](http://doi.wiley.com/10.1029/JA078i034p08087) doi: 10.1029/JA078i034p08087  
 1147 Cai, L., Aikio, A. T., & Nygrn, T. (2014, December). Solar wind effect on Joule  
 1148 heating in the highlatitude ionosphere. *Journal of Geophysical Research: Space*  
 1149 *Physics*, *119*(12). Retrieved 2022-11-20, from [https://onlinelibrary.wiley](https://onlinelibrary.wiley.com/doi/abs/10.1002/2014JA020269)  
 1150 [.com/doi/abs/10.1002/2014JA020269](https://onlinelibrary.wiley.com/doi/abs/10.1002/2014JA020269) doi: 10.1002/2014JA020269  
 1151 Carbary, J. F., Sotirelis, T., Newell, P., & Meng, C.-I. (2003). Auroral bound-  
 1152 ary correlations between UVI and DMSP. *Journal of Geophysical Research*,  
 1153 *108*(A1), 1018. Retrieved 2022-11-01, from [http://doi.wiley.com/10.1029/](http://doi.wiley.com/10.1029/2002JA009378)  
 1154 [2002JA009378](http://doi.wiley.com/10.1029/2002JA009378) doi: 10.1029/2002JA009378  
 1155 Carter, J. A., Milan, S. E., Paxton, L. J., Anderson, B. J., & Gjerloev, J. (2020).  
 1156 Heightintegrated ionospheric conductances parameterized by interplanetary  
 1157 magnetic field and substorm phase. *Journal of Geophysical Research: Space*  
 1158 *Physics*, *125*(10). Retrieved 2022-11-10, from [https://onlinelibrary.wiley](https://onlinelibrary.wiley.com/doi/10.1029/2020JA028121)  
 1159 [.com/doi/10.1029/2020JA028121](https://onlinelibrary.wiley.com/doi/10.1029/2020JA028121) doi: 10.1029/2020JA028121  
 1160 Connor, H. K., Zesta, E., Ober, D. M., & Raeder, J. (2014). The relation between  
 1161 transpolar potential and reconnection rates during sudden enhancement of  
 1162 solar wind dynamic pressure: OpenGGCM-CTIM results. *Journal of Geophys-*  
 1163 *ical Research: Space Physics*, *119*(5), 3411–3429. Retrieved from [https://](https://agupubs.onlinelibrary.wiley.com/doi/abs/10.1002/2013JA019728)  
 1164 [agupubs.onlinelibrary.wiley.com/doi/abs/10.1002/2013JA019728](https://agupubs.onlinelibrary.wiley.com/doi/abs/10.1002/2013JA019728) doi:  
 1165 10.1002/2013JA019728  
 1166 Cowley, S. W. H., & Lockwood, M. (1992). Excitation and decay of solar wind-  
 1167 driven flows in the magnetosphere-ionosphere system. *Annales Geophysicae*,  
 1168 *10*, 103–115. Retrieved 2022-08-18, from [https://ui.adsabs.harvard.edu/](https://ui.adsabs.harvard.edu/abs/1992AnGeo..10..103C)  
 1169 [abs/1992AnGeo..10..103C](https://ui.adsabs.harvard.edu/abs/1992AnGeo..10..103C) (ADS Bibcode: 1992AnGeo..10..103C)  
 1170 Dang, T., Li, X., Luo, B., Li, R., Zhang, B., Pham, K., ... Wang, Y. (2022).  
 1171 Unveiling the space weather during the Starlink satellites destruction event  
 1172 on 4 February 2022. *Space Weather*, *20*(8). Retrieved 2022-10-23, from  
 1173 <https://onlinelibrary.wiley.com/doi/10.1029/2022SW003152> doi:  
 1174 10.1029/2022SW003152  
 1175 Danilov, A. A., Krymskii, G. F., & Makarov, G. A. (2013). Geomagnetic  
 1176 activity as a reflection of processes in the magnetospheric tail: 1. The  
 1177 source of diurnal and semiannual variations in geomagnetic activity. *Ge-*  
 1178 *omagnetism and Aeronomy*, *53*(4), 441–447. Retrieved 2022-11-03,  
 1179 from <http://link.springer.com/10.1134/S0016793213040051> doi:  
 1180 10.1134/S0016793213040051  
 1181 DeJong, A. D., Cai, X., Clauer, R. C., & Spann, J. F. (2007). Aurora and  
 1182 open magnetic flux during isolated substorms, sawteeth, and SMC events.

- 1183 *Annales Geophysicae*, 25(8), 1865–1876. Retrieved 2022-10-28, from  
 1184 <https://angeo.copernicus.org/articles/25/1865/2007/> doi: 10.5194/  
 1185 angeo-25-1865-2007
- 1186 Elphinstone, R. D., Murphree, J. S., Hearn, D. J., Heikkila, W., Henderson,  
 1187 M. G., Cogger, L. L., & Sandahl, I. (1993). The auroral distribution  
 1188 and its mapping according to substorm phase. *Journal of Atmospheric*  
 1189 *and Terrestrial Physics*, 55(14), 1741–1762. Retrieved 2022-10-23, from  
 1190 <https://linkinghub.elsevier.com/retrieve/pii/002191699390142L>  
 1191 doi: 10.1016/0021-9169(93)90142-L
- 1192 Fang, T., Kubaryk, A., Goldstein, D., Li, Z., FullerRowell, T., Millward, G., ...  
 1193 Babcock, E. (2022). Space weather environment during the SpaceX Starlink  
 1194 satellite loss in February 2022. *Space Weather*. Retrieved 2022-11-05, from  
 1195 <https://onlinelibrary.wiley.com/doi/10.1029/2022SW003193> doi:  
 1196 10.1029/2022SW003193
- 1197 Finch, I. D., & Lockwood, M. (2007). Solar wind-magnetosphere coupling functions  
 1198 on timescales of 1 day to 1 year. *Annales Geophysicae*, 25(2), 495–506. Re-  
 1199 trieved 2022-08-18, from [https://angeo.copernicus.org/articles/25/495/](https://angeo.copernicus.org/articles/25/495/2007/)  
 1200 2007/ doi: 10.5194/angeo-25-495-2007
- 1201 Finch, I. D., Lockwood, M. L., & Rouillard, A. P. (2008). Effects of solar wind mag-  
 1202 netosphere coupling recorded at different geomagnetic latitudes: Separation  
 1203 of directly-driven and storage/release systems. *Geophysical Research Letters*,  
 1204 35(21), L21105. Retrieved 2022-08-18, from [http://doi.wiley.com/10.1029/](http://doi.wiley.com/10.1029/2008GL035399)  
 1205 2008GL035399 doi: 10.1029/2008GL035399
- 1206 Frster, M., & Haaland, S. (2015). Interhemispheric differences in ionospheric  
 1207 convection: Cluster EDI observations revisited. *Journal of Geophysical*  
 1208 *Research: Space Physics*, 120(7), 5805–5823. Retrieved 2022-10-23, from  
 1209 <https://onlinelibrary.wiley.com/doi/10.1002/2014JA020774> doi:  
 1210 10.1002/2014JA020774
- 1211 Gjerloev, J. W. (2012). The SuperMAG data processing technique. *Jour-*  
 1212 *nal of Geophysical Research: Space Physics*, 117(A9), n/a–n/a. Retrieved  
 1213 2022-11-06, from <http://doi.wiley.com/10.1029/2012JA017683> doi:  
 1214 10.1029/2012JA017683
- 1215 Grocott, A., Cowley, S. W. H., Sigwarth, J. B., Watermann, J. F., & Yeoman, T. K.  
 1216 (2002). Excitation of twin-vortex flow in the nightside high-latitude ionosphere  
 1217 during an isolated substorm. *Annales Geophysicae*, 20(10), 1577–1601. Re-  
 1218 trieved 2022-10-25, from [https://angeo.copernicus.org/articles/20/](https://angeo.copernicus.org/articles/20/1577/2002/)  
 1219 1577/2002/ doi: 10.5194/angeo-20-1577-2002
- 1220 Hairston, M. R., & Heelis, R. A. (1990). Model of the high-latitude ionospheric  
 1221 convection pattern during southward interplanetary magnetic field using  
 1222 DE 2 data. *Journal of Geophysical Research*, 95(A3), 2333. Retrieved  
 1223 2022-10-23, from <http://doi.wiley.com/10.1029/JA095iA03p02333> doi:  
 1224 10.1029/JA095iA03p02333
- 1225 Hajra, S., Dashora, N., & Ivan, J. S. (2022). On the sources, coupling and energetics  
 1226 during supersubstorms of the solar cycle 24. *Journal of Geophysical Research:*  
 1227 *Space Physics*, 127(10). Retrieved 2022-11-12, from [https://onlinelibrary](https://onlinelibrary.wiley.com/doi/10.1029/2022JA030604)  
 1228 [.wiley.com/doi/10.1029/2022JA030604](https://onlinelibrary.wiley.com/doi/10.1029/2022JA030604) doi: 10.1029/2022JA030604
- 1229 Hapgood, M. A., Liu, H., & Lugaz, N. (2022). SpaceXsailing close to the  
 1230 space weather? *Space Weather*, 20(3). Retrieved 2022-11-05, from  
 1231 <https://onlinelibrary.wiley.com/doi/10.1029/2022SW003074> doi:  
 1232 10.1029/2022SW003074
- 1233 Hapgood, M. A., & Lockwood, M. (1993). On the voltage and distance across the  
 1234 low latitude boundary layer. *Geophysical Research Letters*, 20(2), 145–148. Re-  
 1235 trieved 2022-08-18, from <http://doi.wiley.com/10.1029/93GL00063> doi: 10  
 1236 .1029/93GL00063
- 1237 Holzer, R. E., McPherron, R. L., & Hardy, D. A. (1986). A quantitative empirical

- 1238 model of the magnetospheric flux transfer process. *Journal of Geophysical Re-*  
 1239 *search*, *91*(A3), 3287. Retrieved 2022-11-07, from <http://doi.wiley.com/10>  
 1240 [.1029/JA091iA03p03287](https://doi.org/10.1029/JA091iA03p03287) doi: 10.1029/JA091iA03p03287
- 1241 Hones, E. W. J., Craven, J. D., Frank, L. A., Evans, D. S., & Newell, P. T. (1989).  
 1242 The horse-collar aurora: A frequent pattern of the aurora in quiet times.  
 1243 *Geophysical Research Letters*, *16*(1), 37-40. Retrieved from [https://](https://agupubs.onlinelibrary.wiley.com/doi/abs/10.1029/GL016i001p00037)  
 1244 [agupubs.onlinelibrary.wiley.com/doi/abs/10.1029/GL016i001p00037](https://agupubs.onlinelibrary.wiley.com/doi/abs/10.1029/GL016i001p00037)  
 1245 doi: 10.1029/GL016i001p00037
- 1246 Hubert, B., Blockx, C., Milan, S. E., & Cowley, S. W. H. (2009). Statistical prop-  
 1247 erties of flux closure induced by solar wind dynamic pressure fronts. *Jour-*  
 1248 *nal of Geophysical Research: Space Physics*, *114*(A7), n/a–n/a. Retrieved  
 1249 2022-11-11, from <http://doi.wiley.com/10.1029/2008JA013813> doi:  
 1250 10.1029/2008JA013813
- 1251 Imber, S. M., Milan, S. E., & Hubert, B. (2006). The auroral and ionospheric flow  
 1252 signatures of dual lobe reconnection. *Annales Geophysicae*, *24*(11), 3115–3129.  
 1253 Retrieved 2022-10-23, from [https://angeo.copernicus.org/articles/24/](https://angeo.copernicus.org/articles/24/3115/2006/)  
 1254 [3115/2006/](https://angeo.copernicus.org/articles/24/3115/2006/) doi: 10.5194/angeo-24-3115-2006
- 1255 Kabin, K., Rankin, R., Rostoker, G., Marchand, R., Rae, I. J., Ridley, A. J., ... L.,  
 1256 D. D. (2004). Open-closed field line boundary position: A parametric study  
 1257 using an MHD model. *Journal of Geophysical Research*, *109*(A5), A05222.  
 1258 Retrieved 2022-10-27, from <http://doi.wiley.com/10.1029/2003JA010168>  
 1259 doi: 10.1029/2003JA010168
- 1260 Kalafatoglu, E. E. C., Kaymaz, Z., Frissell, N. A., Ruohoniemi, J. M., & Rasttter, L.  
 1261 (2018). Investigating upper atmospheric joule heating using crosscombination  
 1262 of data for two moderate substorm cases. *Space Weather*, *16*(8), 987–1012. Re-  
 1263 trieved 2022-11-20, from [https://onlinelibrary.wiley.com/doi/10.1029/](https://onlinelibrary.wiley.com/doi/10.1029/2018SW001956)  
 1264 [2018SW001956](https://onlinelibrary.wiley.com/doi/10.1029/2018SW001956) doi: 10.1029/2018SW001956
- 1265 Karlsson, S. B. P., Opgenoorth, H. J., Eglitis, P., Kauristie, K., Syrjsuo, M.,  
 1266 Pulkkinen, T., ... Romanov, S. (2000). Solar wind control of magneto-  
 1267 spheric energy content: Substorm quenching and multiple onsets. *Journal*  
 1268 *of Geophysical Research: Space Physics*, *105*(A3), 5335–5356. Retrieved  
 1269 2022-08-18, from <http://doi.wiley.com/10.1029/1999JA900297> doi:  
 1270 10.1029/1999JA900297
- 1271 Kataoka, R., Shiota, D., Fujiwara, H., Jin, H., Tao, C., Shinagawa, H., & Miyoshi,  
 1272 Y. (2022). Unexpected space weather causing the reentry of 38 Starlink  
 1273 satellites in february 2022. *EartharXiv preprint*. Retrieved 2022-11-05, from  
 1274 <https://eartharxiv.org/repository/object/3208/download/6447/> doi:  
 1275 10.31223/X5GH0X
- 1276 King, J. H., & Papitashvili, N. E. (2005). Solar wind spatial scales in and com-  
 1277 parisons of hourly wind and ACE plasma and magnetic field data. *J. Geophys.*  
 1278 *Res.*, *110*, A02104. Retrieved from <https://doi.org/10.1029/2004JA010649>  
 1279 doi: 10.1029/2004JA010649
- 1280 Kivelson, M. G., & Hughes, W. J. (1990). On the threshold for triggering substorms.  
 1281 *Planetary and Space Science*, *38*(2), 211–220. Retrieved 2022-11-03, from  
 1282 <https://linkinghub.elsevier.com/retrieve/pii/0032063390900855> doi:  
 1283 10.1016/0032-0633(90)90085-5
- 1284 Kokubun, S., McPherron, R. L., & Russell, C. T. (1977). Triggering of substorms by  
 1285 solar wind discontinuities. *Journal of Geophysical Research*, *82*(1), 74–86. Re-  
 1286 trieved 2022-11-11, from <http://doi.wiley.com/10.1029/JA082i001p00074>  
 1287 doi: 10.1029/JA082i001p00074
- 1288 Koochak, Z., & FraserSmith, A. C. (2017). An update on the centered and eccentric  
 1289 geomagnetic dipoles and their poles for the years 19802015. *Earth and Space*  
 1290 *Science*, *4*(10), 626–636. Retrieved 2022-10-27, from [https://onlinelibrary](https://onlinelibrary.wiley.com/doi/10.1002/2017EA000280)  
 1291 [.wiley.com/doi/10.1002/2017EA000280](https://onlinelibrary.wiley.com/doi/10.1002/2017EA000280) doi: 10.1002/2017EA000280
- 1292 Kubyshkina, M., Tsyganenko, N., Semenov, V., Kubyshkina, D., Partamies, N., &

- 1293 Gordeev, E. (2015). Further evidence for the role of magnetotail current shape  
1294 in substorm initiation. *Earth, Planets and Space*, *67*(1), 139. Retrieved 2022-  
1295 11-03, from <http://www.earth-planets-space.com/content/67/1/139> doi:  
1296 10.1186/s40623-015-0304-1
- 1297 Laundal, K. M., Reistad, J. P., Hatch, S. M., Moretto, T., Ohma, A., stgaard,  
1298 N., ... Kloss, C. (2020). Time-scale dependence of solar wind-based re-  
1299 gression models of ionospheric electrodynamics. *Scientific Reports*, *10*(1),  
1300 16406. Retrieved 2022-10-23, from [https://www.nature.com/articles/  
1301 s41598-020-73532-z](https://www.nature.com/articles/s41598-020-73532-z) doi: 10.1038/s41598-020-73532-z
- 1302 Lee, D.-Y. (2004). Sawtooth oscillations directly driven by solar wind dynamic pres-  
1303 sure enhancements. *Journal of Geophysical Research*, *109*(A4), A04202. Re-  
1304 trieved 2022-11-11, from <http://doi.wiley.com/10.1029/2003JA010246> doi:  
1305 10.1029/2003JA010246
- 1306 Li, H., Jiang, W., Wang, C., Verscharen, D., Zeng, C., Russell, C. T., ... Burch,  
1307 J. L. (2020). Evolution of the Earth's magnetosheath turbulence: A Statistical  
1308 study based on MMS observations. *The Astrophysical Journal*, *898*(2), L43.  
1309 Retrieved 2022-11-18, from [https://iopscience.iop.org/article/10.3847/  
1310 2041-8213/aba531](https://iopscience.iop.org/article/10.3847/2041-8213/aba531) doi: 10.3847/2041-8213/aba531
- 1311 Liu, J., Wang, W., Zhang, B., Huang, C., & Lin, . (2018). Temporal variation of  
1312 solar wind in controlling solar windmagnetosphereionosphere energy budget.  
1313 *Journal of Geophysical Research: Space Physics*, *123*(7), 5862–5869. Re-  
1314 trieved 2022-11-11, from [https://onlinelibrary.wiley.com/doi/10.1029/  
1315 2017JA025154](https://onlinelibrary.wiley.com/doi/10.1029/2017JA025154) doi: 10.1029/2017JA025154
- 1316 Lockwood, M. (1991). On flow reversal boundaries and transpolar voltage in aver-  
1317 age models of high-latitude convection. *Planetary and Space Science*, *39*(3),  
1318 397–409. Retrieved 2022-08-18, from [https://linkinghub.elsevier.com/  
1319 retrieve/pii/003206339190002R](https://linkinghub.elsevier.com/retrieve/pii/003206339190002R) doi: 10.1016/0032-0633(91)90002-R
- 1320 Lockwood, M. (2013). Reconstruction and prediction of variations in the open solar  
1321 magnetic flux and interplanetary conditions. *Living Reviews in Solar Physics*,  
1322 *10*, 4. Retrieved from <https://doi.org/10.12942/lrsp-2013-4> doi: 10  
1323 .12942/lrsp-2013-4
- 1324 Lockwood, M. (2022). Solar windmagnetosphere coupling functions: Pitfalls, lim-  
1325 itations, and applications. *Space Weather*, *20*(2). Retrieved 2022-05-27,  
1326 from <https://onlinelibrary.wiley.com/doi/10.1029/2021SW002989> doi:  
1327 10.1029/2021SW002989
- 1328 Lockwood, M., Bentley, S. N., Owens, M. J., Barnard, L. A., Scott, C. J., Watt,  
1329 C. E., & Allanson, O. (2019). The development of a space climatology: 1.  
1330 Solar wind magnetosphere coupling as a function of timescale and the effect  
1331 of data gaps. *Space Weather*, *17*(1), 133–156. Retrieved 2022-08-18, from  
1332 <https://onlinelibrary.wiley.com/doi/abs/10.1029/2018SW001856> doi:  
1333 10.1029/2018SW001856
- 1334 Lockwood, M., Chambodut, A., Finch, I. D., Barnard, L. A., Owens, M. J., &  
1335 Haines, C. (2019). Time-of-day/time-of-year response functions of plane-  
1336 tary geomagnetic indices. *Journal of Space Weather and Space Climate*, *9*,  
1337 A20. Retrieved 2022-08-18, from [https://www.swsc-journal.org/10.1051/  
1338 swsc/2019017](https://www.swsc-journal.org/10.1051/swsc/2019017) doi: 10.1051/swsc/2019017
- 1339 Lockwood, M., & Cowley, S. W. H. (2022). Magnetosphere-ionosphere coupling:  
1340 Implications of non-equilibrium conditions. *Frontiers in Astronomy and Space  
1341 Sciences*, *9*, 908571. Retrieved 2022-08-18, from [https://www.frontiersin  
1342 .org/articles/10.3389/fspas.2022.908571/full](https://www.frontiersin.org/articles/10.3389/fspas.2022.908571/full) doi: 10.3389/fspas.2022  
1343 .908571
- 1344 Lockwood, M., Cowley, S. W. H., & Freeman, M. P. (1990). The excitation of  
1345 plasma convection in the high-latitude ionosphere. *Journal of Geophysical  
1346 Research*, *95*(A6), 7961. Retrieved 2022-08-18, from [http://doi.wiley.com/  
1347 10.1029/JA095iA06p07961](http://doi.wiley.com/10.1029/JA095iA06p07961) doi: 10.1029/JA095iA06p07961

- 1348 Lockwood, M., Haines, C., Barnard, L. A., Owens, M. J., Scott, C. J., Cham-  
 1349 bodut, A., & McWilliams, K. A. (2021). Semi-annual, annual and Uni-  
 1350 versal Time variations in the magnetosphere and in geomagnetic activ-  
 1351 ity: 4. Polar cap motions and origins of the Universal Time effect. *Jour-  
 1352 nal of Space Weather and Space Climate*, *11*, 15. Retrieved 2022-08-18,  
 1353 from <https://www.swsc-journal.org/10.1051/swsc/2020077> doi:  
 1354 10.1051/swsc/2020077
- 1355 Lockwood, M., Hairston, M., Finch, I. D., & Rouillard, A. P. (2009). Transpolar  
 1356 voltage and polar cap flux during the substorm cycle and steady convection  
 1357 events. *Journal of Geophysical Research: Space Physics*, *114*(A1), n/a–n/a.  
 1358 Retrieved 2022-08-18, from <http://doi.wiley.com/10.1029/2008JA013697>  
 1359 doi: 10.1029/2008JA013697
- 1360 Lockwood, M., Lanchester, B. S., Morley, S. K., Throp, K., Milan, S. E., Lester,  
 1361 M., & Frey, H. U. (2006). Modeling the observed proton aurora and iono-  
 1362 spheric convection responses to changes in the IMF clock angle: 2. Persistence  
 1363 of ionospheric convection. *Journal of Geophysical Research*, *111*(A2), A02306.  
 1364 Retrieved 2022-08-18, from <http://doi.wiley.com/10.1029/2003JA010307>  
 1365 doi: 10.1029/2003JA010307
- 1366 Lockwood, M., & McWilliams, K. A. (2021a). On optimum solar windmagneto-  
 1367 sphere coupling functions for transpolar voltage and planetary geomagnetic  
 1368 activity. *Journal of Geophysical Research: Space Physics*, *126*(12). Re-  
 1369 trieved 2022-05-28, from [https://onlinelibrary.wiley.com/doi/10.1029/  
 1370 2021JA029946](https://onlinelibrary.wiley.com/doi/10.1029/2021JA029946) doi: 10.1029/2021JA029946
- 1371 Lockwood, M., & McWilliams, K. A. (2021b). A survey of 25 years' transpolar volt-  
 1372 age data from the SuperDARN radar network and the expandingcontracting  
 1373 polar cap model. *Journal of Geophysical Research: Space Physics*, *126*(9). Re-  
 1374 trieved 2022-08-18, from [https://onlinelibrary.wiley.com/doi/10.1029/  
 1375 2021JA029554](https://onlinelibrary.wiley.com/doi/10.1029/2021JA029554) doi: 10.1029/2021JA029554
- 1376 Lockwood, M., McWilliams, K. A., Owens, M. J., Barnard, L. A., Watt, C. E.,  
 1377 Scott, C. J., ... Coxon, J. C. (2020). Semi-annual, annual and Universal Time  
 1378 variations in the magnetosphere and in geomagnetic activity: 2. Response to  
 1379 solar wind power input and relationships with solar wind dynamic pressure  
 1380 and magnetospheric flux transport. *Journal of Space Weather and Space Cli-  
 1381 mate*, *10*, 30. Retrieved 2022-08-18, from [https://www.swsc-journal.org/  
 1382 10.1051/swsc/2020033](https://www.swsc-journal.org/10.1051/swsc/2020033) doi: 10.1051/swsc/2020033
- 1383 Lockwood, M., & Milan, S. E. (2023). Universal Time variations in the magneto-  
 1384 sphere. *Frontiers in Astronomy and Space Sciences*, *10*, in press.
- 1385 Lockwood, M., & Morley, S. K. (2004). A numerical model of the ionospheric sig-  
 1386 natures of time-varying magnetic reconnection: 1. Ionospheric convection. *An-  
 1387 nales Geophysicae*, *22*(1), 73–91. Retrieved 2022-08-18, from [https://angeo  
 1388 .copernicus.org/articles/22/73/2004/](https://angeo.copernicus.org/articles/22/73/2004/) doi: 10.5194/angeo-22-73-2004
- 1389 Lockwood, M., Owens, M. J., Barnard, L. A., Haines, C., Scott, C. J., McWilliams,  
 1390 K. A., & Coxon, J. C. (2020). Semi-annual, annual and Universal Time vari-  
 1391 ations in the magnetosphere and in geomagnetic activity: 1. Geomagnetic  
 1392 data. *Journal of Space Weather and Space Climate*, *10*, 23. Retrieved 2022-  
 1393 08-18, from <https://www.swsc-journal.org/10.1051/swsc/2020023> doi:  
 1394 10.1051/swsc/2020023
- 1395 Lockwood, M., Owens, M. J., Barnard, L. A., Scott, C. J., Frost, A. M., Yu,  
 1396 B., & Chi, Y. (2022). Application of historic datasets to understand-  
 1397 ing open solar flux and the 20th-century grand solar maximum. 1. Geo-  
 1398 magnetic, ionospheric, and sunspot observations. *Frontiers in Astron-  
 1399 omy and Space Sciences*, *9*, 960775. Retrieved 2022-09-01, from [https://  
 1400 www.frontiersin.org/articles/10.3389/fspas.2022.960775/full](https://www.frontiersin.org/articles/10.3389/fspas.2022.960775/full) doi:  
 1401 10.3389/fspas.2022.960775
- 1402 Lockwood, M., Owens, M. J., Barnard, L. A., Watt, C. E., Scott, C. J., Coxon,

- 1403 J. C., & McWilliams, K. A. (2020). Semi-annual, annual and Universal Time  
1404 variations in the magnetosphere and in geomagnetic activity: 3. Modelling.  
1405 *Journal of Space Weather and Space Climate*, *10*, 61. Retrieved 2022-08-  
1406 18, from <https://www.swsc-journal.org/10.1051/swsc/2020062> doi:  
1407 10.1051/swsc/2020062
- 1408 Lockwood, M., Rouillard, A. P., Finch, I. D., & Stamper, R. (2006). Comment  
1409 on the *IDV* index: Its derivation and use in inferring long-term variations  
1410 of the interplanetary magnetic field strength by Leif Svalgaard and Edward  
1411 W. Cliver. *Journal of Geophysical Research*, *111*(A9), A09109. Retrieved  
1412 2022-08-18, from <http://doi.wiley.com/10.1029/2006JA011640> doi:  
1413 10.1029/2006JA011640
- 1414 Longden, N., Chisham, G., Freeman, M. P., Abel, G. A., & Sotirelis, T. (2010).  
1415 Estimating the location of the open-closed magnetic field line boundary from  
1416 auroral images. *Annales Geophysicae*, *28*(9), 1659–1678. Retrieved 2022-11-  
1417 01, from <https://angeo.copernicus.org/articles/28/1659/2010/> doi:  
1418 10.5194/angeo-28-1659-2010
- 1419 Lukianova, R. (2003). Magnetospheric response to sudden changes in solar wind dy-  
1420 namic pressure inferred from polar cap index. *Journal of Geophysical Research*,  
1421 *108*(A12), 1428. Retrieved 2022-11-11, from [http://doi.wiley.com/10.1029/](http://doi.wiley.com/10.1029/2002JA009790)  
1422 [2002JA009790](http://doi.wiley.com/10.1029/2002JA009790) doi: 10.1029/2002JA009790
- 1423 Lhr, H., Lockwood, M., Sandholt, P. E., Hansen, T. L., & Moretto, T. (1996).  
1424 Multi-instrument ground-based observations of a travelling convection vor-  
1425 tices event. *Annales Geophysicae*, *14*(2), 162–181. Retrieved 2022-08-18,  
1426 from <https://angeo.copernicus.org/articles/14/162/1996/> doi:  
1427 10.1007/s00585-996-0162-z
- 1428 Mayaud, P.-N. (1972). The aa indices: A 100-year series characterizing the magnetic  
1429 activity. *J. Geophys. Res.*, *77*(34), 6870–6874. Retrieved from [https://doi](https://doi.org/10.1029/ja077i034p06870)  
1430 [.org/10.1029/ja077i034p06870](https://doi.org/10.1029/ja077i034p06870) doi: 10.1029/ja077i034p06870
- 1431 Milan, S. E., Boakes, P. D., & Hubert, B. (2008). Response of the expand-  
1432 ing/contracting polar cap to weak and strong solar wind driving: Implications  
1433 for substorm onset. *Journal of Geophysical Research: Space Physics*, *113*(A9),  
1434 n/a–n/a. Retrieved 2022-10-23, from [http://doi.wiley.com/10.1029/](http://doi.wiley.com/10.1029/2008JA013340)  
1435 [2008JA013340](http://doi.wiley.com/10.1029/2008JA013340) doi: 10.1029/2008JA013340
- 1436 Milan, S. E., Carter, J. A., Bower, G. E., Imber, S. M., Paxton, L. J., Anderson,  
1437 B. J., ... Hubert, B. (2020). Duallobe reconnection and horsecollar auroras.  
1438 *Journal of Geophysical Research: Space Physics*, *125*(10). Retrieved 2022-10-  
1439 23, from <https://onlinelibrary.wiley.com/doi/10.1029/2020JA028567>  
1440 doi: 10.1029/2020JA028567
- 1441 Milan, S. E., Carter, J. A., Korth, H., & Anderson, B. J. (2015). Principal com-  
1442 ponent analysis of Birkeland currents determined by the Active Magneto-  
1443 sphere and Planetary Electrodynamics Response Experiment. *Journal of*  
1444 *Geophysical Research: Space Physics*, *120*(12), 10,415–10,424. Retrieved  
1445 2022-11-12, from <http://doi.wiley.com/10.1002/2015JA021680> doi:  
1446 10.1002/2015JA021680
- 1447 Milan, S. E., Carter, J. A., Sangha, H., Bower, G. E., & Anderson, B. J. (2021).  
1448 Magnetospheric flux throughput in the Dungey cycle: Identification of con-  
1449 vection state during 2010. *Journal of Geophysical Research: Space Physics*,  
1450 *126*(2), e2020JA028437. Retrieved from [https://agupubs.onlinelibrary](https://agupubs.onlinelibrary.wiley.com/doi/abs/10.1029/2020JA028437)  
1451 [.wiley.com/doi/abs/10.1029/2020JA028437](https://agupubs.onlinelibrary.wiley.com/doi/abs/10.1029/2020JA028437) doi: [https://doi.org/10.1029/](https://doi.org/10.1029/2020JA028437)  
1452 [2020JA028437](https://doi.org/10.1029/2020JA028437)
- 1453 Milan, S. E., Carter, J. A., Sangha, H., Laundal, K. M., stgaard, N., Tenfjord, P.,  
1454 ... Anderson, B. J. (2018). Timescales of dayside and nightside field-aligned  
1455 current response to changes in solar wind-magnetosphere coupling. *Jour-*  
1456 *nal of Geophysical Research: Space Physics*, *123*(9), 7307–7319. Retrieved  
1457 2022-11-12, from <http://doi.wiley.com/10.1029/2018JA025645> doi:

- 1458 10.1029/2018JA025645  
 1459 Milan, S. E., Clausen, L. B. N., Coxon, J. C., Carter, J. A., Walach, M.-T., Laun-  
 1460 dal, K., ... Anderson, B. J. (2017). Overview of solar windmagnetosphere  
 1461 ionosphereatmosphere coupling and the generation of magnetospheric cur-  
 1462 rents. *Space Science Reviews*, 206(1-4), 547–573. Retrieved 2022-10-23,  
 1463 from <http://link.springer.com/10.1007/s11214-017-0333-0> doi:  
 1464 10.1007/s11214-017-0333-0
- 1465 Milan, S. E., Provan, G., & Hubert, B. (2007). Magnetic flux transport in the  
 1466 Dungey cycle: A survey of dayside and nightside reconnection rates. *Jour-  
 1467 nal of Geophysical Research: Space Physics*, 112(A1), n/a–n/a. Retrieved  
 1468 2022-10-24, from <http://doi.wiley.com/10.1029/2006JA011642> doi:  
 1469 10.1029/2006JA011642
- 1470 Mishin, V., & Karavaev, Y. (2017). Saturation of the magnetosphere dur-  
 1471 ing superstorms: New results from the magnetogram inversion technique.  
 1472 *Solar-Terrestrial Physics*, 3(3), 28–36. Retrieved 2022-10-28, from [http://  
 1473 naukaru.ru/en/nauka/article/18490/view](http://naukaru.ru/en/nauka/article/18490/view) doi: 10.12737/stp-33201704
- 1474 Morley, S. K., & Lockwood, M. (2005). A numerical model of the ionospheric sig-  
 1475 natures of time-varying magnetic reconnection: 2. Measuring expansions in the  
 1476 ionospheric flow response. *Annales Geophysicae*, 23(7), 2501–2510. Retrieved  
 1477 2022-08-18, from <https://angeo.copernicus.org/articles/23/2501/2005/>  
 1478 doi: 10.5194/angeo-23-2501-2005
- 1479 Newell, P. T., & Gjerloev, J. W. (2011). Evaluation of SuperMAG auroral electro-  
 1480 jet indices as indicators of substorms and auroral power. *Journal of Geophysi-  
 1481 cal Research: Space Physics*, 116(A12), 2011JA016779. Retrieved 2022-11-06,  
 1482 from <https://onlinelibrary.wiley.com/doi/10.1029/2011JA016779> doi:  
 1483 10.1029/2011JA016779
- 1484 Newell, P. T., & Meng, C.-I. (1989). Dipole tilt angle effects on the lati-  
 1485 tude of the cusp and cleft/low-latitude boundary layer. *Journal of Geo-  
 1486 physical Research: Space Physics*, 94(A6), 6949–6953. Retrieved 2022-  
 1487 10-27, from <http://doi.wiley.com/10.1029/JA094iA06p06949> doi:  
 1488 10.1029/JA094iA06p06949
- 1489 Owens, M. J., Lockwood, M., & Barnard, L. A. (2020). The value of CME arrival  
 1490 time forecasts for space weather mitigation. *Space Weather*, 18(9). Re-  
 1491 trieved 2022-08-18, from [https://onlinelibrary.wiley.com/doi/10.1029/  
 1492 2020SW002507](https://onlinelibrary.wiley.com/doi/10.1029/2020SW002507) doi: 10.1029/2020SW002507
- 1493 Palmroth, M. (2004). Role of solar wind dynamic pressure in driving ionospheric  
 1494 Joule heating. *Journal of Geophysical Research*, 109(A11), A11302. Retrieved  
 1495 2022-11-11, from <http://doi.wiley.com/10.1029/2004JA010529> doi:  
 1496 10.1029/2004JA010529
- 1497 Paxton, L. J., Morrison, D., Zhang, Y., Kil, H., Wolven, B., Ogorzalek, B. S., ...  
 1498 Meng, C.-I. (2002). Validation of remote sensing products produced by the  
 1499 Special Sensor Ultraviolet Scanning Imager (SSUSI): a far UV-imaging spec-  
 1500 trograph on DMSP F-16. In A. M. Larar & M. G. Mlynczak (Eds.), (pp.  
 1501 338–348). San Diego, CA. Retrieved 2022-11-01, from [http://proceedings  
 1502 .spiedigitallibrary.org/proceeding.aspx?articleid=893287](http://proceedings.spiedigitallibrary.org/proceeding.aspx?articleid=893287) doi:  
 1503 10.1117/12.454268
- 1504 Paxton, L. J., Zhang, Y., Kil, H., & Schaefer, R. K. (2021). Exploring the up-  
 1505 per atmosphere: Using optical remote sensing. In W. Wang, Y. Zhang, &  
 1506 L. J. Paxton (Eds.), *Geophysical monograph series* (1st ed., pp. 487–522). Wi-  
 1507 ley. Retrieved 2022-11-01, from [https://onlinelibrary.wiley.com/doi/  
 1508 10.1002/9781119815631.ch23](https://onlinelibrary.wiley.com/doi/10.1002/9781119815631.ch23) doi: 10.1002/9781119815631.ch23
- 1509 Picone, J. M., Hedin, A. E., Drob, D. P., & Aikin, A. C. (2002). NRLMSISE-  
 1510 00 empirical model of the atmosphere: Statistical comparisons and scientific  
 1511 issues. *Journal of Geophysical Research: Space Physics*, 107(A12), SIA 15–  
 1512 1–SIA 15–16. Retrieved 2022-11-05, from <http://doi.wiley.com/10.1029/>

- 1513 2002JA009430 doi: 10.1029/2002JA009430
- 1514 Richmond, A. D., Ridley, E. C., & Roble, R. G. (1992). A thermosphere/ionosphere  
1515 general circulation model with coupled electrodynamics. *Geophysical Research*  
1516 *Letters*, 19(6), 601–604. Retrieved 2022-11-06, from [http://doi.wiley.com/](http://doi.wiley.com/10.1029/92GL00401)  
1517 10.1029/92GL00401 doi: 10.1029/92GL00401
- 1518 Ridley, A. J., Gombosi, T. I., & DeZeeuw, D. L. (2004). Ionospheric control of the  
1519 magnetosphere: conductance. *Annales Geophysicae*, 22(2), 567–584. Retrieved  
1520 2022-11-10, from <https://angeo.copernicus.org/articles/22/567/2004/>  
1521 doi: 10.5194/angeo-22-567-2004
- 1522 Robinson, R. M., & Zanetti, L. J. (2021). Auroral energy flux and joule heating de-  
1523 rived from global maps of fieldaligned currents. *Geophysical Research Letters*,  
1524 48(7). Retrieved 2022-11-01, from [https://onlinelibrary.wiley.com/doi/](https://onlinelibrary.wiley.com/doi/10.1029/2020GL091527)  
1525 10.1029/2020GL091527 doi: 10.1029/2020GL091527
- 1526 Russell, C. T., & McPherron, R. L. (1973). Semiannual variation of geomagnetic  
1527 activity. *Journal of Geophysical Research*, 78(1), 92–108. Retrieved 2022-11-  
1528 03, from <http://doi.wiley.com/10.1029/JA078i001p00092> doi: 10.1029/  
1529 JA078i001p00092
- 1530 Sandhu, J. K., Rae, I. J., & Walach, M. (2021). Challenging the use of ring current  
1531 indices during geomagnetic storms. *Journal of Geophysical Research: Space*  
1532 *Physics*, 126(2). Retrieved 2022-11-01, from [https://onlinelibrary.wiley](https://onlinelibrary.wiley.com/doi/10.1029/2020JA028423)  
1533 [.com/doi/10.1029/2020JA028423](https://onlinelibrary.wiley.com/doi/10.1029/2020JA028423) doi: 10.1029/2020JA028423
- 1534 Schieldge, J., & Siscoe, G. (1970). A correlation of the occurrence of simultaneous  
1535 sudden magnetospheric compressions and geomagnetic bay onsets with selected  
1536 geophysical indices. *Journal of Atmospheric and Terrestrial Physics*, 32(11),  
1537 1819–1830. Retrieved 2022-11-11, from [https://linkinghub.elsevier.com/](https://linkinghub.elsevier.com/retrieve/pii/002191697090139X)  
1538 [retrieve/pii/002191697090139X](https://linkinghub.elsevier.com/retrieve/pii/002191697090139X) doi: 10.1016/0021-9169(70)90139-X
- 1539 Shukhtina, M. A., Dmitrieva, N. P., Popova, N. G., Sergeev, V. A., Yahnin,  
1540 A. G., & Despirak, I. V. (2005). Observational evidence of the loading-  
1541 unloading substorm scheme. *Geophysical Research Letters*, 32(17). Retrieved  
1542 2022-11-11, from <http://doi.wiley.com/10.1029/2005GL023779> doi:  
1543 10.1029/2005GL023779
- 1544 Siscoe, G. L. (1982). Polar cap size and potential: A predicted relationship. *Geo-*  
1545 *physical Research Letters*, 9(6), 672–675. Retrieved 2022-10-23, from [http://](http://doi.wiley.com/10.1029/GL009i006p00672)  
1546 [doi.wiley.com/10.1029/GL009i006p00672](http://doi.wiley.com/10.1029/GL009i006p00672) doi: 10.1029/GL009i006p00672
- 1547 Sivadas, N., & Sibeck, D. (2022). Regression bias in using solar wind measure-  
1548 ments. *Frontiers in Astronomy and Space Sciences*, 9, 924976. Retrieved  
1549 2022-07-07, from [https://www.frontiersin.org/articles/10.3389/](https://www.frontiersin.org/articles/10.3389/fspas.2022.924976/full)  
1550 [fspas.2022.924976/full](https://www.frontiersin.org/articles/10.3389/fspas.2022.924976/full) doi: 10.3389/fspas.2022.924976
- 1551 Smith, M. F., & Lockwood, M. (1996). Earth’s magnetospheric cusps. *Reviews*  
1552 *of Geophysics*, 34(2), 233–260. Retrieved 2022-08-18, from [http://doi.wiley](http://doi.wiley.com/10.1029/96RG00893)  
1553 [.com/10.1029/96RG00893](http://doi.wiley.com/10.1029/96RG00893) doi: 10.1029/96RG00893
- 1554 Southwood, D. J. (1987). The ionospheric signature of flux transfer events. *Journal*  
1555 *of Geophysical Research*, 92(A4), 3207. Retrieved 2022-11-11, from [http://](http://doi.wiley.com/10.1029/JA092iA04p03207)  
1556 [doi.wiley.com/10.1029/JA092iA04p03207](http://doi.wiley.com/10.1029/JA092iA04p03207) doi: 10.1029/JA092iA04p03207
- 1557 Stauning, P., & Troshichev, O. A. (2008). Polar cap convection and PC index dur-  
1558 ing sudden changes in solar wind dynamic pressure. *Journal of Geophysical Re-*  
1559 *search: Space Physics*, 113(A8), n/a–n/a. Retrieved 2022-11-11, from [http://](http://doi.wiley.com/10.1029/2007JA012783)  
1560 [doi.wiley.com/10.1029/2007JA012783](http://doi.wiley.com/10.1029/2007JA012783) doi: 10.1029/2007JA012783
- 1561 Stubbs, T. J., R., V. R., stgaard N., B., S. J., & A., F. L. (2005). Simulta-  
1562 neous observations of the auroral ovals in both hemispheres under vary-  
1563 ing conditions. *Geophysical Research Letters*, 32(3), L03103. Retrieved  
1564 2022-10-27, from <http://doi.wiley.com/10.1029/2004GL021199> doi:  
1565 10.1029/2004GL021199
- 1566 Tanaka, T. (2007). Magnetosphereionosphere convection as a compound system.  
1567 *Space Science Reviews*, 133(1-4), 1–72. Retrieved 2022-11-10, from <https://>

- 1568 [link.springer.com/10.1007/s11214-007-9168-4](https://link.springer.com/10.1007/s11214-007-9168-4) doi: 10.1007/s11214-007-9168-4
- 1569
- 1570 Tsurutani, B. T., Green, J. L., & Hajra, R. (2022). The possible cause of the 40  
1571 SpaceX Starlink satellite losses in February 2022: Prompt penetrating electric  
1572 fields and the dayside equatorial and midlatitude ionospheric convective up-  
1573 lift. *arXiv preprint*. Retrieved 2022-11-05, from [https://arxiv.org/pdf/](https://arxiv.org/pdf/2210.07902)  
1574 [2210.07902](https://arxiv.org/pdf/2210.07902) doi: 10.48550/arXiv.2210.07902
- 1575 Tsyganenko, N. A. (2019). Secular drift of the auroral ovals: How fast do they  
1576 actually move? *Geophysical Research Letters*, *46*(6), 3017–3023. Retrieved  
1577 2022-10-27, from [https://onlinelibrary.wiley.com/doi/abs/10.1029/](https://onlinelibrary.wiley.com/doi/abs/10.1029/2019GL082159)  
1578 [2019GL082159](https://onlinelibrary.wiley.com/doi/abs/10.1029/2019GL082159) doi: 10.1029/2019GL082159
- 1579 Tulegenov, B., Raeder, J., Cramer, W. D., Ferdousi, B., Fuller-Rowell, T. J.,  
1580 Maruyama, N., & Strangeway, R. J. (2023). Storm time polar cap expansion:  
1581 interplanetary magnetic field clock angle dependence. *Annales Geophysicae*,  
1582 *41*(1), 39–54. Retrieved 2023-01-20, from [https://angeo.copernicus.org/](https://angeo.copernicus.org/articles/41/39/2023/)  
1583 [articles/41/39/2023/](https://angeo.copernicus.org/articles/41/39/2023/) doi: 10.5194/angeo-41-39-2023
- 1584 Vorobjev, V. G., & Yagodkina, O. I. (2010). Seasonal and UT variations of  
1585 the position of the auroral precipitation and polar cap boundaries. *Geo-*  
1586 *magnetism and Aeronomy*, *50*(5), 597–605. Retrieved 2022-10-27,  
1587 from <http://link.springer.com/10.1134/S0016793210050063> doi:  
1588 [10.1134/S0016793210050063](http://link.springer.com/10.1134/S0016793210050063)
- 1589 Walach, M.-T., Milan, S. E., Yeoman, T. K., Hubert, B. A., & Hairston, M. R.  
1590 (2017). Testing nowcasts of the ionospheric convection from the expanding  
1591 and contracting polar cap model. *Space Weather*, *15*(4), 623–636. Retrieved  
1592 2022-10-25, from <http://doi.wiley.com/10.1002/2017SW001615> doi:  
1593 [10.1002/2017SW001615](http://doi.wiley.com/10.1002/2017SW001615)
- 1594 Wang, X.-Y., Zhang, Q.-H., Wang, C., Zhang, Y.-L., Tang, B., Xing, Z.-Y., ...  
1595 Wang, Y. (2022). An almost complete disappearance of open-flux polar cap for  
1596 strongly northward interplanetary magnetic field. *Commun. Earth Environ.*,  
1597 In Review. Retrieved 2022-10-23, from [https://www.researchsquare.com/](https://www.researchsquare.com/article/rs-1246727/v1)  
1598 [article/rs-1246727/v1](https://www.researchsquare.com/article/rs-1246727/v1) doi: 10.21203/rs.3.rs-1246727/v1
- 1599 Weimer, D. R. (2005). Improved ionospheric electrodynamic models and appli-  
1600 cation to calculating Joule heating rates. *Journal of Geophysical Research*,  
1601 *110*(A5), A05306. Retrieved 2022-11-06, from [http://doi.wiley.com/](http://doi.wiley.com/10.1029/2004JA010884)  
1602 [10.1029/2004JA010884](http://doi.wiley.com/10.1029/2004JA010884) doi: 10.1029/2004JA010884
- 1603 Wilson, G. R., Weimer, D. R., Wise, J. O., & Marcos, F. A. (2006). Response of  
1604 the thermosphere to Joule heating and particle precipitation. *Journal of Geo-*  
1605 *physical Research*, *111*(A10), A10314. Retrieved 2022-11-06, from [http://doi](http://doi.wiley.com/10.1029/2005JA011274)  
1606 [.wiley.com/10.1029/2005JA011274](http://doi.wiley.com/10.1029/2005JA011274) doi: 10.1029/2005JA011274
- 1607 Yamazaki, Y., & Maute, A. (2017). Sq and EEJ a review on the daily vari-  
1608 ation of the geomagnetic field caused by ionospheric dynamo currents.  
1609 *Space Science Reviews*, *206*(1-4), 299–405. Retrieved 2022-10-30, from  
1610 <http://link.springer.com/10.1007/s11214-016-0282-z> doi: 10.1007/  
1611 [s11214-016-0282-z](http://link.springer.com/10.1007/s11214-016-0282-z)
- 1612 Yue, C., Zong, Q. G., Zhang, H., Wang, Y. F., Yuan, C. J., Pu, Z. Y., ... Wang,  
1613 C. R. (2010). Geomagnetic activity triggered by interplanetary shocks. *Jour-*  
1614 *nal of Geophysical Research: Space Physics*, *115*(A5), n/a–n/a. Retrieved  
1615 2022-11-11, from <http://doi.wiley.com/10.1029/2010JA015356> doi:  
1616 [10.1029/2010JA015356](http://doi.wiley.com/10.1029/2010JA015356)
- 1617 Zhang, X., Wang, C., Chen, T., Wang, Y. L., Tan, A., Wu, T. S., ... Wang,  
1618 W. (2005). Global patterns of Joule heating in the high-latitude iono-  
1619 sphere. *Journal of Geophysical Research*, *110*(A12), A12208. Retrieved  
1620 2022-11-20, from <http://doi.wiley.com/10.1029/2005JA011222> doi:  
1621 [10.1029/2005JA011222](http://doi.wiley.com/10.1029/2005JA011222)
- 1622 Zhang, Y., Paxton, L. J., Schaefer, R., & Swartz, W. H. (2022). Thermospheric

1623 conditions associated with the loss of 40 Starlink satellites. *Space Weather*,  
1624 *20*(10). Retrieved 2022-10-29, from [https://onlinelibrary.wiley.com/doi/](https://onlinelibrary.wiley.com/doi/10.1029/2022SW003168)  
1625 [10.1029/2022SW003168](https://onlinelibrary.wiley.com/doi/10.1029/2022SW003168) doi: 10.1029/2022SW003168  
1626 ye, S. (2018). *Parametrization of the nightside reconnection rate during times with*  
1627 *contracting polar caps* (Master's thesis, Department of Physics, University  
1628 of Oslo, Norway). Retrieved 2022-11-03, from [https://www.duo.uio.no/](https://www.duo.uio.no/bitstream/handle/10852/64071/8/Master.pdf)  
1629 [bitstream/handle/10852/64071/8/Master.pdf](https://www.duo.uio.no/bitstream/handle/10852/64071/8/Master.pdf)

## 1630 8 Open Research

1631 The data used in this study are all openly available. The interplanetary data are  
1632 available from the Physics Data Facility (SPDF) at NASA's Goddard Space Flight Cen-  
1633 ter as the Omni composite from [https://omniweb.gsfc.nasa.gov/ow\\_min.html](https://omniweb.gsfc.nasa.gov/ow_min.html). The  
1634 am indices are available from the International Service of Geomagnetic Indices (ISGI)  
1635 at [http://isgi.unistra.fr/data\\_download.php](http://isgi.unistra.fr/data_download.php). The SuperMAG SML and SMR in-  
1636 dices are available from the SuperMAG project website at the Johns Hopkins Univer-  
1637 sity Applied Physics Laboratory at <http://supermag.jhuapl.edu/indices/>. The SYM-  
1638 H index is available from the World Data Center for Geomagnetism, Kyoto at [http://](http://wdc.kugi.kyoto-u.ac.jp/)  
1639 [wdc.kugi.kyoto-u.ac.jp/](http://wdc.kugi.kyoto-u.ac.jp/). The Kp geomagnetic index is available from Geomagnetic  
1640 Observatory Niemegk, GFZ German Research Centre for Geosciences at [https://www](https://www-app3.gfz-potsdam.de/kp_index/Kp_ap_since_1932.txt)  
1641 [-app3.gfz-potsdam.de/kp\\_index/Kp\\_ap\\_since\\_1932.txt](https://www-app3.gfz-potsdam.de/kp_index/Kp_ap_since_1932.txt) The DMSP SSUSI images  
1642 are available from the SSUSI project website at the Johns Hopkins University Applied  
1643 Physics Laboratory <http://ssusi.jhuapl.edu/>.

## 1644 Acknowledgments

1645 The authors are grateful to the many instrument scientists and engineers who make  
1646 the datasets employed in this study possible and the staff of a number of datacentres who  
1647 allow easy access to the data. These include: the Space Physics Data Facility (SPDF)  
1648 at NASA's Goddard Space Flight Center for the Omni composite of interplanetary ob-  
1649 servations; the International Service of Geomagnetic Indices (ISGI), France and collab-  
1650 orating institutes for the am geomagnetic indices; the World Data Center for Geomag-  
1651 netism, Kyoto for the SYM-H index; the PIs and staff of the many groups contributing  
1652 data to the SuperMAG project, coordinated at The Johns Hopkins University Applied  
1653 Physics Laboratory, for the SMR and SML indices; The Geomagnetic Observatory Niemegk,  
1654 GFZ German Research Centre for Geosciences for the Kp index; The Air Force Defense  
1655 Meteorological Satellite Program (DMSP) and, in particular, the Special Sensor Ultra-  
1656 violet Spectrographic Imagers (SSUSI) project at The Johns Hopkins University Applied  
1657 Physics Laboratory. This work is supported by a number of grants: consolidated grants  
1658 number ST/R000921/1 and ST/V000497/1 from the United Kingdom Science and Tech-  
1659 nology Facilities Council (UKRI/STFC) and the SWIGS Directed Highlight Topic Grant  
1660 number NE/P016928/1/ and grant NE/S010033/1 from the United Kingdom Natural  
1661 Environment Research Council (UKRI/NERC). The authors are also grateful to Steve  
1662 Milan for valuable discussions of this work.